

## Overview of the Mars Pathfinder Mission: Launch through landing, surface operations, data sets, and science results

M. P. Golombek,<sup>1</sup> R. C. Anderson,<sup>1</sup> J. R. Barnes,<sup>2</sup> J. F. Bell III,<sup>3</sup> N. T. Bridges,<sup>1</sup> D. T. Britt,<sup>4</sup> J. Brückner,<sup>5</sup> R. A. Cook,<sup>1</sup> D. Crisp,<sup>1</sup> J. A. Crisp,<sup>1</sup> T. Economou,<sup>6</sup> W. M. Folkner,<sup>1</sup> R. Greeley,<sup>7</sup> R. M. Haberle,<sup>8</sup> R. B. Hargraves,<sup>9</sup> J. A. Harris,<sup>1</sup> A. F. C. Haldemann,<sup>1</sup> K. E. Herkenhoff,<sup>1</sup> S. F. Hviid,<sup>10</sup> R. Jaumann,<sup>11</sup> J. R. Johnson,<sup>12</sup> P. H. Kalleymeyn,<sup>1</sup> H. U. Keller,<sup>13</sup> R. L. Kirk,<sup>12</sup> J. M. Knudsen,<sup>10</sup> S. Larsen,<sup>14</sup> M. T. Lemmon,<sup>4</sup> M. B. Madsen,<sup>10</sup> J. A. Magalhães,<sup>8</sup> J. N. Maki,<sup>1</sup> M. C. Malin,<sup>15</sup> R. M. Manning,<sup>1</sup> J. Matijevic,<sup>1</sup> H. Y. McSween Jr.,<sup>16</sup> H. J. Moore,<sup>17</sup> S. L. Murchie,<sup>18</sup> J. R. Murphy,<sup>8</sup> T. J. Parker,<sup>1</sup> R. Rieder,<sup>5</sup> T. P. Rivellini,<sup>1</sup> J. T. Schofield,<sup>1</sup> A. Seiff,<sup>8</sup> R. B. Singer,<sup>4</sup> P. H. Smith,<sup>4</sup> L. A. Soderblom,<sup>12</sup> D. A. Spencer,<sup>1</sup> C. R. Stoker,<sup>8</sup> R. Sullivan,<sup>3</sup> N. Thomas,<sup>13</sup> S. W. Thurman,<sup>1</sup> M. G. Tomasko,<sup>4</sup> R. M. Vaughan,<sup>1</sup> H. Wänke,<sup>5</sup> A. W. Ward,<sup>12</sup> and G. R. Wilson,<sup>7</sup>

**Abstract.** Mars Pathfinder successfully landed at Ares Vallis on July 4, 1997, deployed and navigated a small rover about 100 m clockwise around the lander, and collected data from three science instruments and ten technology experiments. The mission operated for three months and returned 2.3 Gbits of data, including over 16,500 lander and 550 rover images, 16 chemical analyses of rocks and soil, and 8.5 million individual temperature, pressure and wind measurements. Pathfinder is the best known location on Mars, having been clearly identified with respect to other features on the surface by correlating five prominent horizon features and two small craters in lander images with those in high-resolution orbiter images and in inertial space from two-way ranging and Doppler tracking. Tracking of the lander has fixed the spin pole of Mars, determined the precession rate since Viking 20 years ago, and indicates a polar moment of inertia, which constrains a central metallic core to be between 1300 and ~2000 km in radius. Dark rocks appear to be high in silica and geochemically similar to anorogenic andesites; lighter rocks are richer in sulfur and lower in silica, consistent with being coated with various amounts of dust. Rover and lander images show rocks with a variety of morphologies, fabrics and textures, suggesting a variety of rock types are present. Rounded pebbles and cobbles on the surface as well as rounded bumps and pits on some rocks indicate these rocks may be conglomerates (although other explanations are also possible), which almost definitely require liquid water to form and a warmer and wetter past. Airborne dust is composed of composite silicate particles with a small fraction of a highly magnetic mineral, interpreted to be most likely maghemite; explanations suggest iron was dissolved from crustal materials during an active hydrologic cycle with maghemite freeze dried onto silicate dust grains. Remote sensing data at a scale of a kilometer or greater and an Earth analog correctly predicted a rocky plain safe for landing and roving with a variety of rocks deposited by catastrophic floods, which are relatively dust free. The surface appears to have changed little since it formed billions of years ago, with the exception that eolian activity may have deflated the surface by ~3–7 cm, sculpted wind tails, collected sand into dunes, and eroded ventifacts (fluted and grooved rocks). Pathfinder found a dusty lower atmosphere, early morning water ice clouds, and morning near-surface air temperatures that changed abruptly with time and height. Small scale vortices, interpreted to be dust devils, were observed repeatedly in the afternoon by the meteorology instruments and have been imaged.

<sup>1</sup>Jet Propulsion Laboratory, California Institute of Technology, Pasadena

<sup>2</sup>College of Oceanic and Atmospheric Sciences, Oregon State University, Corvallis, Oregon.

<sup>3</sup>Center for Radio Physics and Space Research, Cornell University, Ithaca, New York

<sup>4</sup>Lunar and Planetary Laboratory, University of Arizona, Tucson.

<sup>5</sup>Max-Planck-Institut für Chemie, Mainz, Germany.

<sup>6</sup>University of Chicago, Enrico Fermi Institute, Chicago, Illinois.

<sup>7</sup>Department of Geology, Arizona State University, Tempe.

<sup>8</sup>Ames Research Center, Moffett Field, California.

Copyright 1999 by the American Geophysical Union

Paper number 98JE02554.  
0148-0227/99/98JE-02554\$09.00

<sup>9</sup>Department of Geosciences, Princeton University, Princeton, New Jersey

<sup>10</sup>Niels Bohr Institute, University of Copenhagen, Denmark.

<sup>11</sup>Deutsche Luft und Raumfahrt, German Aerospace Center, Berlin-Adlershof, Germany.

<sup>12</sup>U.S. Geological Survey, Flagstaff, Arizona.

<sup>13</sup>Max-Planck-Institut für Aeronomie, Katlenburg-Lindau, Germany

<sup>14</sup>Riso National Laboratory, Roskilde, Denmark

<sup>15</sup>Malin Space Science Systems, San Diego, California

<sup>16</sup>Department of Geological Sciences, University of Tennessee, Knoxville

<sup>17</sup>U.S. Geological Survey, Menlo Park, California. Deceased [September 21, 1998]

<sup>18</sup>Applied Physics Laboratory, Johns Hopkins University, Laurel, Maryland

## 1. Introduction

Mars Pathfinder, the first low-cost, quick Discovery class mission to be completed, successfully landed on the surface of Mars on July 4, 1997, deployed and navigated a small rover, and collected data from three science instruments and 10 technology experiments. Although designed primarily as an entry, descent, and landing demonstration [Golombek, 1997], the mission operated on the surface of Mars for 3 months (well beyond the nominal 1 month lander and 1 week rover missions) and returned 2.3 Gbits of new data, including over 16,500 lander and 550 rover images, 16 chemical analyses of rocks and soil, and 8.5 million individual temperature, pressure, and wind measurements. The rover (named Sojourner) traversed 100 m clockwise around the lander (named the Sagan Memorial Station), exploring about 200 m<sup>2</sup> of the surface. The mission captured the imagination of the public, garnered front page headlines during the first week of mission operations, and became one of NASA's most popular missions. A total of about 566 million Internet "hits" were registered during the first month of the mission, with 47 million "hits" on July 8 alone, making the Pathfinder landing by far the largest Internet event in history at the time.

Pathfinder was the first mission to deploy a rover on Mars. It carried a chemical analysis instrument (the alpha proton X-ray spectrometer, or APXS [Rieder *et al.*, 1997a]) to characterize the rocks and soils in a landing area over hundreds of square meters on Mars [Rover Team, 1997b]. The combination of spectral imaging of the landing area by the lander camera (the Imager for Mars Pathfinder, or IMP [Smith *et al.*, 1997a]), chemical analyses aboard the rover, and close-up imaging of textures and fabrics with the lander and rover cameras offered the potential of identifying rock petrology and mineralogy, thereby providing a calibration point or "ground truth" for orbital remote sensing observations [Golombek, 1997]. With this payload, a landing site in Ares Vallis was selected because it appeared acceptably safe and offered the prospect of studying a variety of rock types expected to be deposited by catastrophic floods. Such information would address first-order scientific questions such as differentiation of the crust, the development of weathering products, and the nature of the early Martian environment and its subsequent evolution [Golombek *et al.*, 1997a]. The three instruments (IMP, APXS, and the ASI/MET, or Atmospheric Structure Instrument/Meteorology package [Seiff *et al.*, 1997]) and technology experiments and engineering subsystems on the rover and lander allowed seven areas of scientific investigation (see Golombek [1997] for a more complete description of the mission, instruments, and science objectives and investigations): the geology and geomorphology of the surface, mineralogy and geochemistry of rocks and soils, physical properties of surface materials, magnetic properties of airborne dust, atmospheric science including aerosols, and rotational and orbital dynamics of Mars [Folkner *et al.*, 1997a].

## 2. Launch, Cruise, Entry, Descent, and Landing

The spacecraft was launched on a McDonnell Douglas Delta II 7925 expendable launch vehicle on December 4, 1996, at 0158 EST from Cape Canaveral Air Station in Florida (Plate 1 and Figure 1). It was the third day of the 1 month launch period, in which the first attempt was canceled (without a count-

down) due to bad weather and the second attempt was scrubbed a few minutes before launch due to a problem with nonsynchronous computers at the launch site (the launch window was 1 min each day). About 1.5 hours after launch, Pathfinder exited Earth's shadow, with the Sun illuminating the cruise stage solar panels and Sun sensors for the first time. Although current generated from the gallium arsenide solar panels occurred on schedule, Sun presence as detected by two redundant Sun sensors did not occur. These sensors each provided two axes of Sun angle data to the onboard attitude control software and were needed to carry out turns and course corrections during cruise, which were critical for getting to Mars. Within days, it was determined that both Sun sensors had been optically blocked, one partially and the other fully, by residue from a pyrotechnic detonation that had occurred on the upper stage during separation during launch. Spacecraft engineers worked around the clock during a critical period to modify the software to recognize the reduced-quality information that was available from the partially obscured Sun sensor, which allowed operation of the attitude control system and the necessary turns and course corrections during cruise.

The rest of the 7 month cruise to Mars was fairly uneventful (Figure 2), with four trajectory correction maneuvers performed on January 9, 1997, starting at 0740 PST; February 3, 1997, at 1500 PST; May 6, 1997, at 1730 PDT; and June 25, 1997, at 1000 PDT. A fifth trajectory correction maneuver was considered on July 3, 1997, (2000 PDT) and again on July 4 1997, (0200 PDT), just prior to cruise stage separation (Figure 3) because modeling of tracking data suggested that landing would occur toward the southwestern end of the ellipse, near a large streamlined island (Plate 2). After reviewing the various options for the maneuver and the potential hazards at the landing site, the potential risk of such a late maneuver was considered greater than the potential risk of landing on the sides of the island, and no action was taken. The lander came to rest within about 23 km of the center of the ellipse.

The entry, descent, and landing phase of the mission (Figure 3) began 1.5 hours prior to entry when the on-board software took control and vented the coolant that had been circulating around the vehicle to keep the interior electronics and rover cool during the cruise phase of the mission. Cruise stage separation occurred within a fraction of a second of the predicted time, 30 min prior to entry (Figure 3). Accelerometer data indicated that the 2° nutation acquired during coolant venting was reduced to near zero as a result of energy loss during the spring loaded cruise stage separation event.

Radiometric tracking data acquired up to cruise stage separation indicated that the vehicle entered the atmosphere 304 s before landing at an angle of -14.06° from horizontal, within the 1° tolerance of the nominal -14.2° entry angle at the atmospheric entry point, ~130 km above the surface. Atmospheric deceleration peaked at -15.9 g and proceeded on target with only minor variations from the predictions.

Parachute deployment occurred 134 s before landing, only 6 s later than the a priori predicted time at an altitude of 9.4 km (Figure 3). All subsequent events including heat shield separation and lander bridle deployment occurred at the predicted times relative to parachute deployment. The lander took 10 s to descend on the descent rate limiter to the point that the bridle was fully extended and loaded. Radar data were acquired 1.6 km above the surface, 28.7 s before landing. The terminal descent rate just prior to rocket ignition 98 m above the ground, was -61.2 m/s, about 6 m/s faster than predicted but

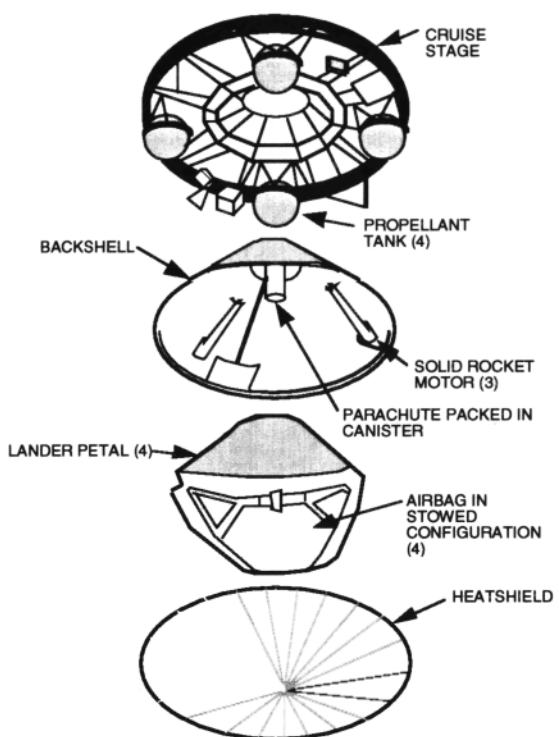


**Figure 1.** Exploded view of Mars Pathfinder flight system, showing back-pack-style cruise stage, backshell with three solid rockets, tetrahedral lander, and aeroshell (heat shield). Diameter of spacecraft is 2.65 m.

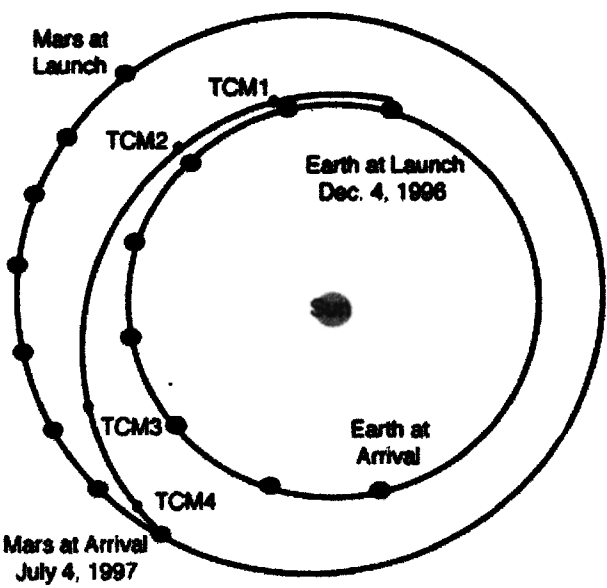


**Figure 2.** Cruise trajectory flown by the Mars Pathfinder spacecraft showing location of Earth and Mars at launch and landing and at 1 month intervals, and the four trajectory correction maneuvers.

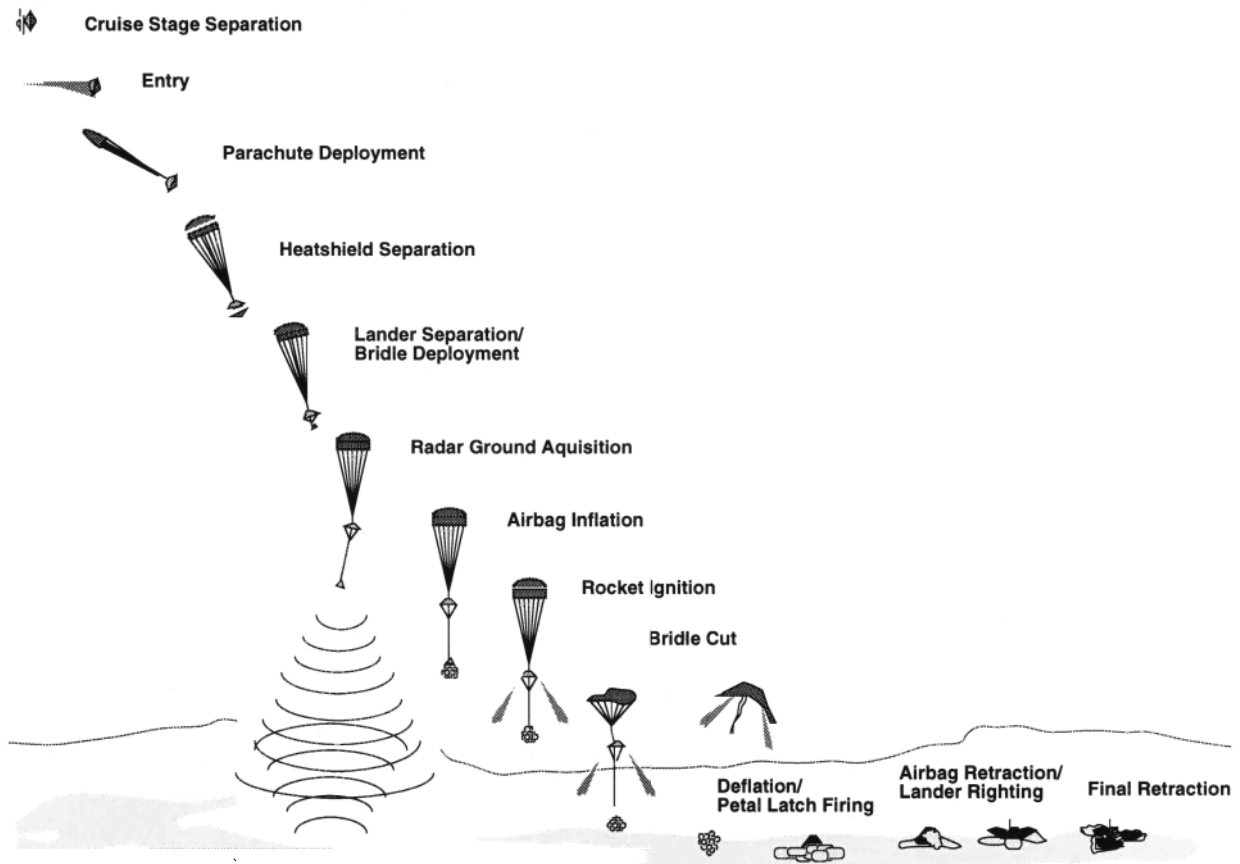


**Figure 3.** Diagram illustrating Mars Pathfinder entry, descent, and landing. Details provided in text.

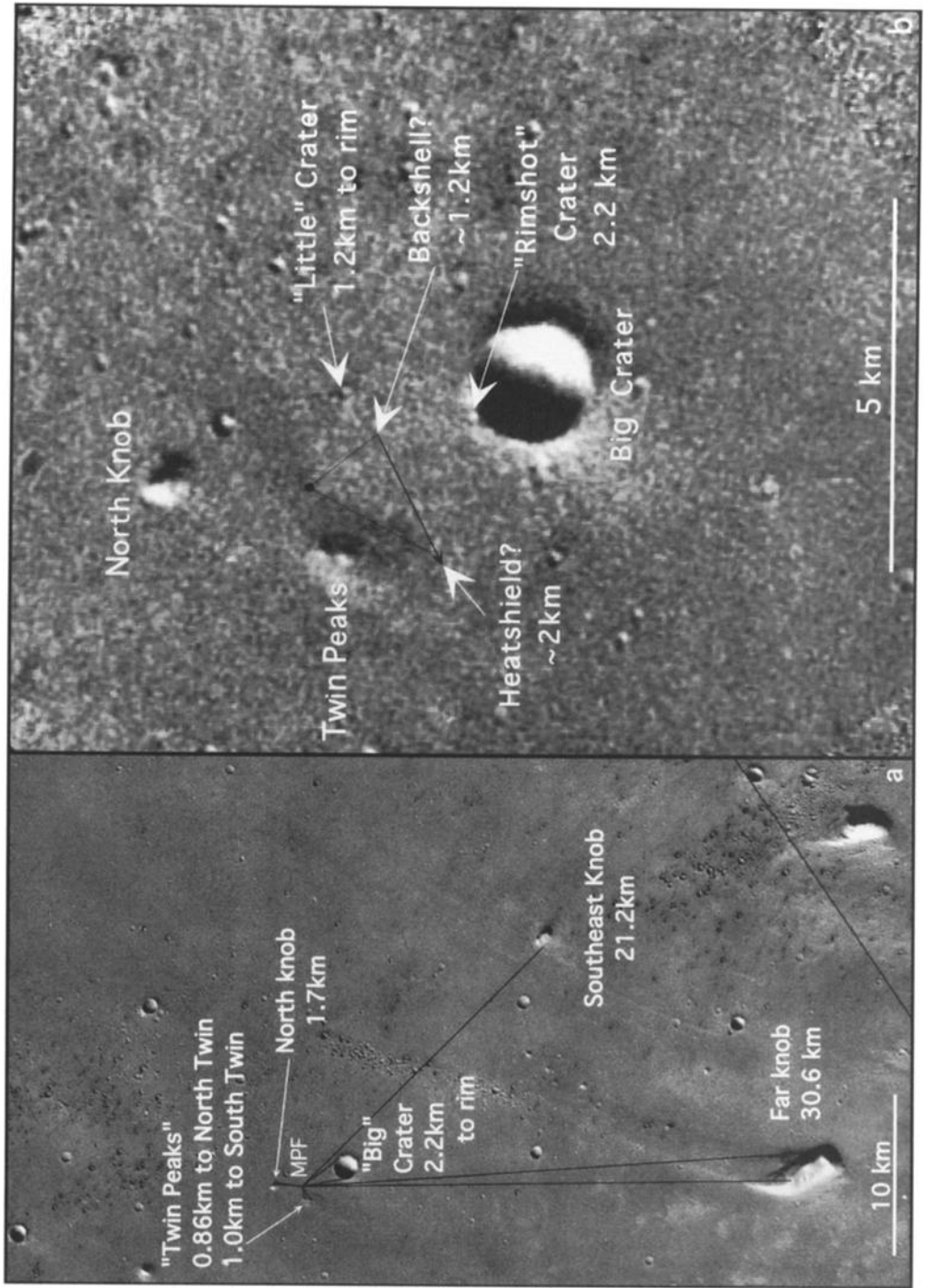


**Figure 4(a).** Location of lander (MPF) in Viking Orbiter images and distances to Big Crater, Far Knob, Southeast Knob, Twin Peaks, and North Knob. (b) Close-up of location of lander in orbiter images showing Twin Peaks, Big Crater, Rimshot Crater, backshell, and heat shield locations. Reconstructions indicate that the solid rockets fired near (or just downrange of) where the backshell is located and the heat shield was carried in a ballistic path about 2 km downrange (west southwest). Winds from the southeast and wind shear resulted in the lander bouncing downhill toward the northwest. Mosaic compiled by co-adding and co-registering Viking stereo images 004A27 and 004A44 and 004A87 and 004A70 to produce a "super resolution" image of the landing site. North is up.

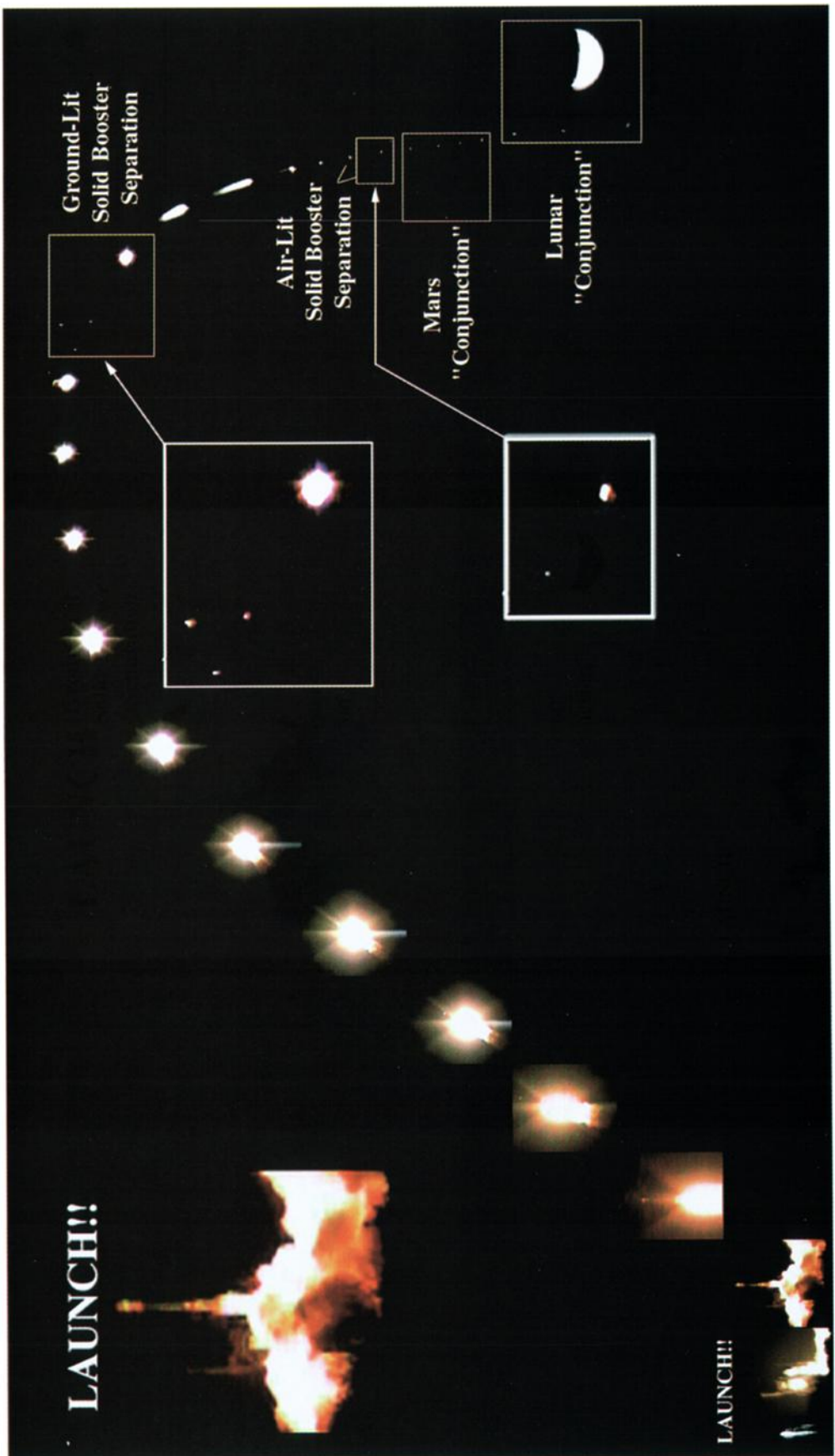


**Plate 1.** Launch of the Mars Pathfinder spacecraft at 0158 on December 4, 1997, from Cape Canaveral Air Station, Florida. Figure shows a time lapse sequence including main rocket ignition, burnout, and jettisoning of the three air-lit solid rockets, and "flyby" of Mars and the Moon. Composite of home video obtained and created by T. Parker, JPL, from Jetty Park, Florida.

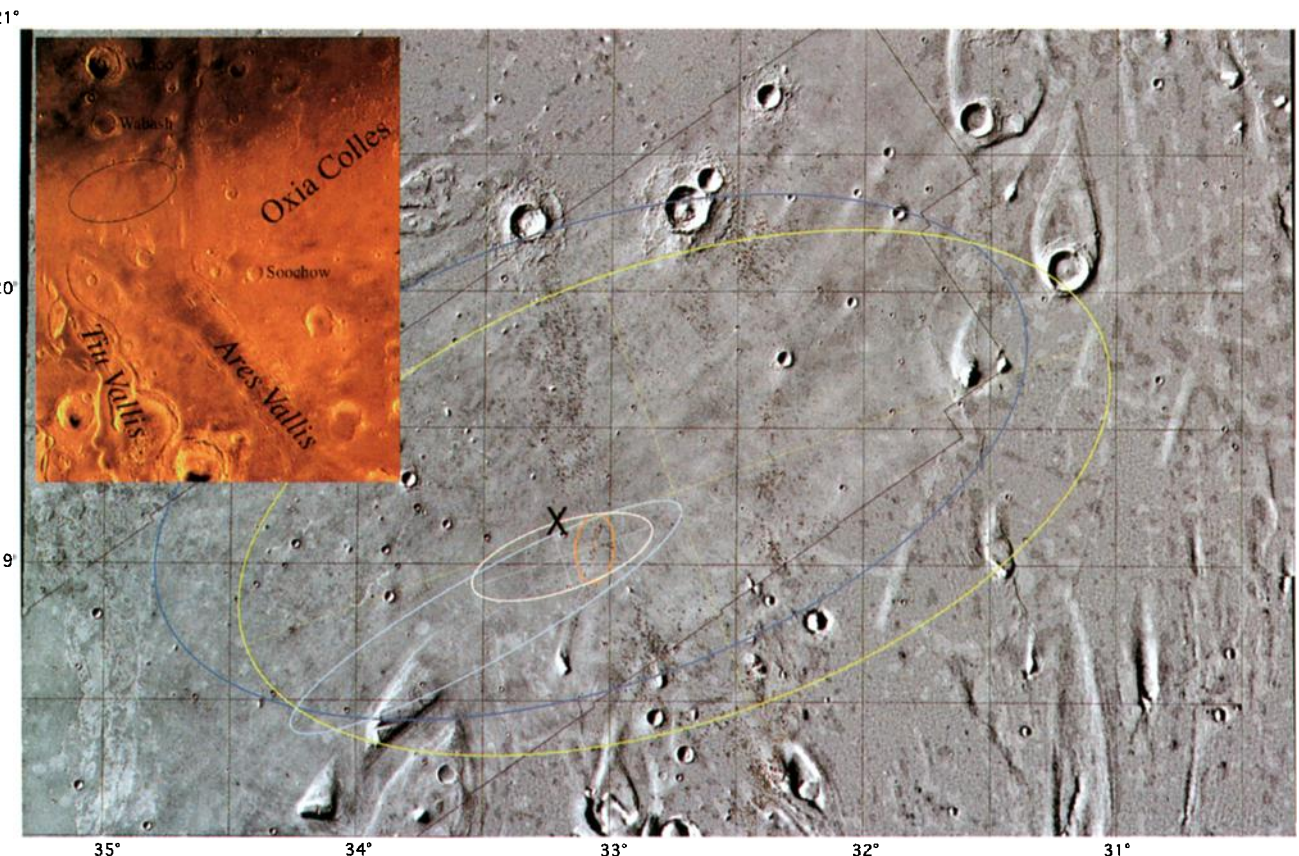


**Plate 2.** Mosaic of Ares Vallis showing different landing ellipses, with color insert of the Chryse Planitia region of Mars that shows the outflow channels. The large blue ellipse (100 by 200 km) to the northwest is an ellipse in the USGS cartographic reference frame (the latitude and longitude shown in this figure) designed to avoid streamlined islands to the south and east, craters to the north, and etched terrain to the west (this ellipse is shown in the color insert). The large yellow ellipse (100 by 200 km) displaced toward the southeast (by 19.82 km in longitude and 11.54 km in latitude) is the navigation target ellipse in the revised local cartographic reference frame [Duxbury, 1995]. The elongate light blue ellipse (98 km by 19 km) is the navigation prediction as of late July 3 and early July 4; it includes part of the streamlined island in the southwest. The smallest (gold) ellipse (15 by 8 km) is the prediction from tracking through atmospheric entry. The second smallest, pink ellipse (41 by 15 km), which encloses the smallest ellipse (and the location of the lander), is the navigation result with dispersions added for atmospheric entry and descent. The black X is the location of the lander with respect to surface features identified in Viking orbiter images (located at 19.13°N, 33.22°W in the USGS reference frame). The location of the lander in inertial space from the two-way ranging and Doppler tracking of the lander is 19.28°N, 33.52°W. If the location of the lander in inertial space is the same as its location with respect to surface features, then the USGS cartographic network is displaced 18.15 km to the west and 8.78 km to the north of the inertial frame, and the local cartographic network is displaced 2.76 km to the south and 1.67 km to the east (3.17 km to the south southeast). Color mosaic is part of the Oxia Palus Quadrangle (MC 11) of Mars; black and white mosaic from Viking orbiter images of 38 m/pixel resolution; north is at the top.

well within design tolerances. Rocket ignition occurred 6.1 s before landing. Lander separation from the bridle, backshell, and parachute occurred 3.8 s before landing, 21.5 m above the ground with a residual initial vertical speed of about +1 m/s. Landing occurred at 0258 true local solar time (0956:55 PDT) at a vertical speed of 14 m/s. This corresponded to a peak initial impact deceleration of 18.7 g, well within the design envelope.

Doppler, accelerometer, and radar based trajectory reconstruction calculations indicate that the lander's horizontal component of the impact velocity was roughly 6 m/s in a north-northwest direction. This horizontal velocity and the calculated ballistic landing point (Figure 4) near Big Crater (see later discussion on the location of the lander) suggest a

horizontal wind from the southeast. Subsequent bounces showed little energy loss, indicating no punctures to the air bags, with 60 s of high rate data samples recording at least 15 bounces. This and the fact that the landing surface is one of the rockiest areas on Mars [e.g., Golombek *et al.*, 1997a, b] demonstrates the robustness of the landing system. Accelerometer and pressure data show that the lander bounced about 10 m downhill during the first minute and traveled about 1 km in a northwest direction (Figure 4). The vehicle rolled to a stop and ended up on its base petal about 2 min after landing. Images from the surface described elsewhere in this paper show what may be the white conical backshell about 1 km southeast of the final landing site, which is consistent with simulations of the backshell trajectory, suggesting that the backshell and

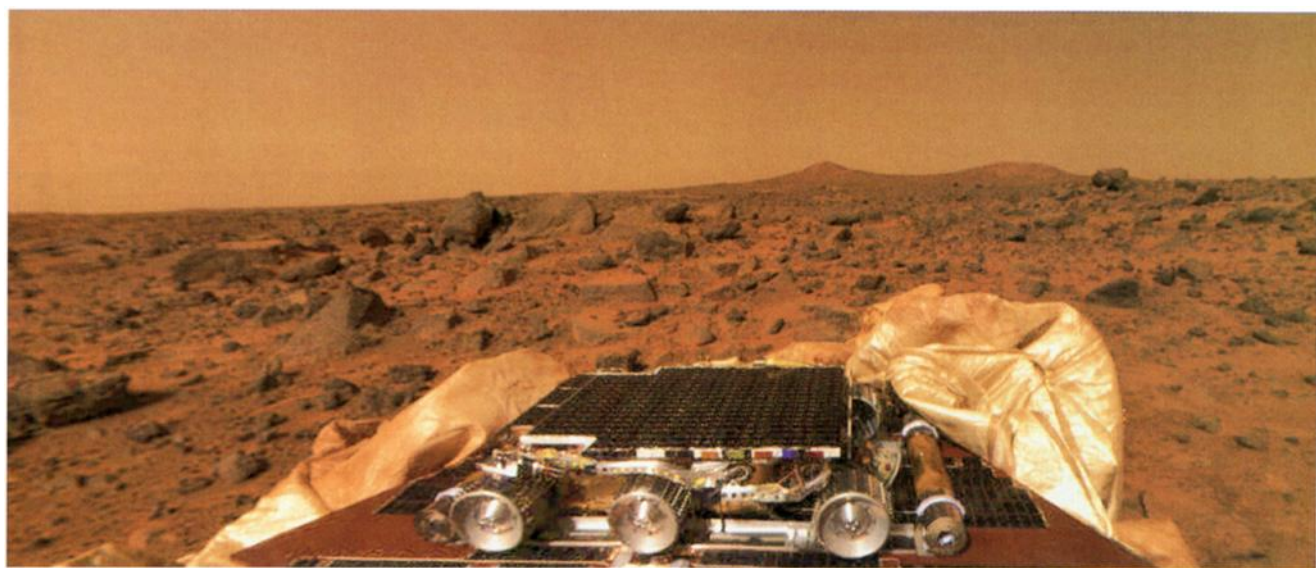


**Plate 3.** Panorama of the Martian surface with dark rocks, bright dust, and light yellowish brown sky at Ares Vallis taken by the IMP on sol 1; the rover is still stowed on the lander petal. Air bag inhibited deployment of the rover ramps (the gold, silver edged cylinders at either end of the rover) and required the petal to be raised and the air bags to be further retracted, prior to rover egress on sol 2. Twin Peaks in the background are about 1 km to the west southwest and contributed to rapid location of the lander in Viking orbiter images. Notice large imbricated or inclined rocks (Shark, Half Dome, and Moe) in the Rock Garden. Color mosaic is made of 24:1 compressed red filter and 48:1 green and blue images.

parachute (Figure 1) would not travel far from the point of rocket ignition (estimated to be near or just downrange of the backshell). If the terminal trajectory did intersect a point to the southeast of the final landing site, trajectory simulations would also indicate that the heat shield (Figure 1) would have come to rest roughly 2 km downrange of the point of rocket ignition (toward the west-southwest, parallel to the principal axis of entry). Images also indicate the possible existence of a bright object in that approximate location southwest of the final landing site (see later discussion). This object may very well be the highly reflective mylar thermal blanketing on the inside surface of the heat shield.

After rolling to a stop, the lander automatically turned off the X-band transmitter to save battery power. Three minutes after landing, air bag retraction began and lasted 72 min. The on-board retraction algorithm used accelerometer measurements to deduce that the lander had rolled onto the base petal. At the moment that retraction began, the lander issued a 45 s radio "blip" or "semaphore" indicating that the lander had come to rest on the base petal and that there was no need to right the lander. Motors inside the lander retracted vectran cords to open a number of 2.5 cm diameter holes (14 in base petal; 23 in other petals) within an interior (lander) facing peel away patch in each air bag for deflation. Each patch was a triangle roughly 45 cm on a side with a vectran mesh scrim (360  $\mu\text{m}$  holes) designed to help keep particulate matter inside the bag. Testing on Earth suggests that most of the deflation of the air bags occurred rapidly, within minutes of patch opening, with the remaining deflation occurring during air bag retraction. After landing on Mars, no obvious exhaust products were identified with the IMP or rover cameras. In tests conducted before launch, contamination external to the air bags was barely no-

ticeable, as a result of the mesh on the peel-away patch holes and the multiple layers of air bag vectran material (inner bladder mesh with up to 220 x 80  $\mu\text{m}$  holes and 360 x 360  $\mu\text{m}$  holes in four outer abrasion resistant layers). Only trace amounts of solid exhaust were found along outer seams of the air bags, and none was found to have escaped through the peel-away patch holes. Tests of air bag inflation and retraction on Earth indicate most of the solid exhaust is composed of sal-ammoniac (ammonium chloride) crystals ( $\text{NH}_4\text{Cl}$ ) ranging in size from a few tenths of a micron to 1 mm, and much of it coats the interior walls of the bags. As a result, little if any solid material from the air bags escaped to contaminate the area around the lander. Exhaust gases produced to inflate the air bags were dominated by carbon monoxide, carbon dioxide, and nitrogen, which would have gone into the atmosphere, with no affect on the surface after being expelled from the bags. Combined with the reconstructions of where the solid rockets fired, the local area where Pathfinder landed must be considered essentially contaminant free (and one of the cleanest landing systems designed, compared with legged landers slowed actively by retrorockets).

Accelerometer data acquired during retraction indicate that the lander tilted almost 20° in the direction of the rock called Mini-Matterhorn (see Plate 4) and almost rolled over, after which the winches slowed due to increased retraction cord loading. (Had the lander rolled over during this process, it would have safely stopped and begun anew, assuming the new orientation, and automatically righted itself.) The lander's petals opened at 81 min after landing, and the radio blip from the low-gain antenna was received at 1134 PDT indicating the successful completion of entry, descent, and landing. Science and engineering accelerometers as well as the pressure and de-

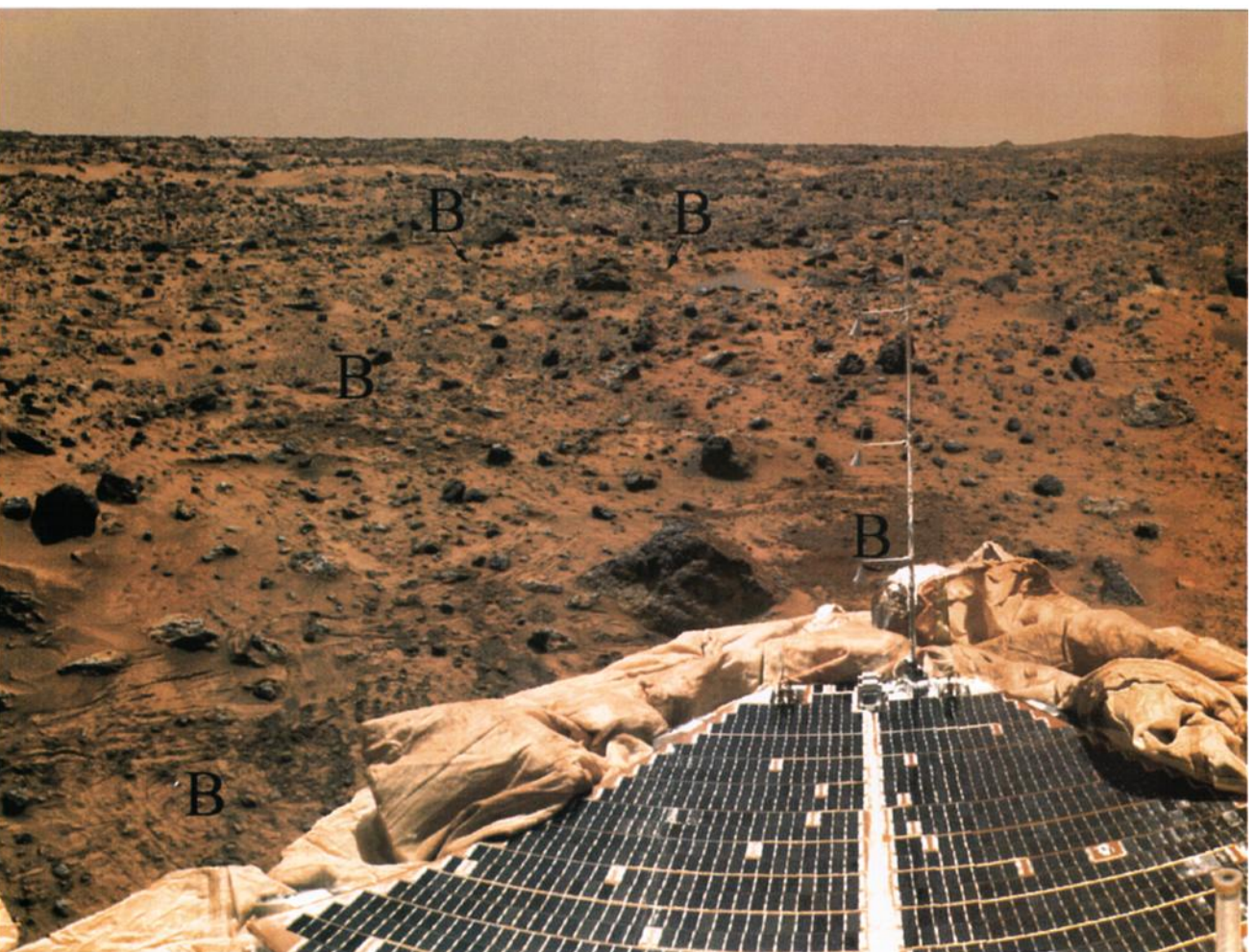


**Plate 4.** Soils disturbed during the last few bounces as the spacecraft approached its final position and subsequently, as the air bags were retracted, appear darker than the surrounding undisturbed soils. The soil darkening suggests a substrate beneath a very thin, relatively bright surface layer that is darker than the surface, or that roughening of the soil surface reduces its reflectivity. Air-bag-retraction marks show as shallow trenches carved by pebbles that were snagged by the air bags. These are found fairly close to the lander. The last air bag bounce marks are roughly circular in shape (foreshortened into ellipses) and are labeled B. The farthest of these, at upper left, is up to 15 m away from the lander. Beyond this point, the surface dips into a broad swale, making positive identification of bounce marks farther from the spacecraft difficult. Pointed rock at edge of petal is Mini-Matterhorn. Accelerometer data indicate the lander tilted 20° in its direction and almost rolled over during air bag retraction, likely due to the air bags momentarily being snagged on the rock. Image cropped from the gallery panorama.

scent temperature sensors acquired data during entry, descent, and landing, which allowed the atmospheric temperature, pressure, and density to be reconstructed [Schofield *et al.*, 1997].

### 3. Lander Surface Location

The actual location of the Mars Pathfinder spacecraft (19.13°N, 33.22°W in the U. S. Geological Survey or USGS reference frame) with respect to surface features on Mars was determined by comparing a mosaic of Viking Orbiter images to surface features and their azimuths identified on the lander's horizon [Golombek *et al.*, 1997b] during the first 2 days of surface operations (Figure 4). Five prominent horizon features were identified (Plate 3 and Figures 5 and 6) and given the informal nicknames: North Knob (azimuth 1°-8°), Southeast

Knob (summit azimuth 135°), Far Knob (azimuth 176°-180°), Twin Peaks (summit azimuths: south peak 242°, north peak 259°-262°), and Big Crater (rim crest azimuth 140°-168°). Images of Twin Peaks were returned during the first high-gain antenna downlink and were so unique that the lander was located and the existence of Big Crater to the southeast was predicted prior to images of it being returned at the end of sol 1. Two small craters are also visible in both the orbiter and lander views. One of these, nicknamed Little Crater (central azimuth 110°, Figure 7), was quickly identified as a crater on the second day of surface operations when the eastern horizon was imaged and the data transmitted to Earth. The second small crater, nicknamed Rimshot Crater (central azimuth 155°), was not recognized for some time after it had been imaged because, rather than showing the distinctive profile of a crater

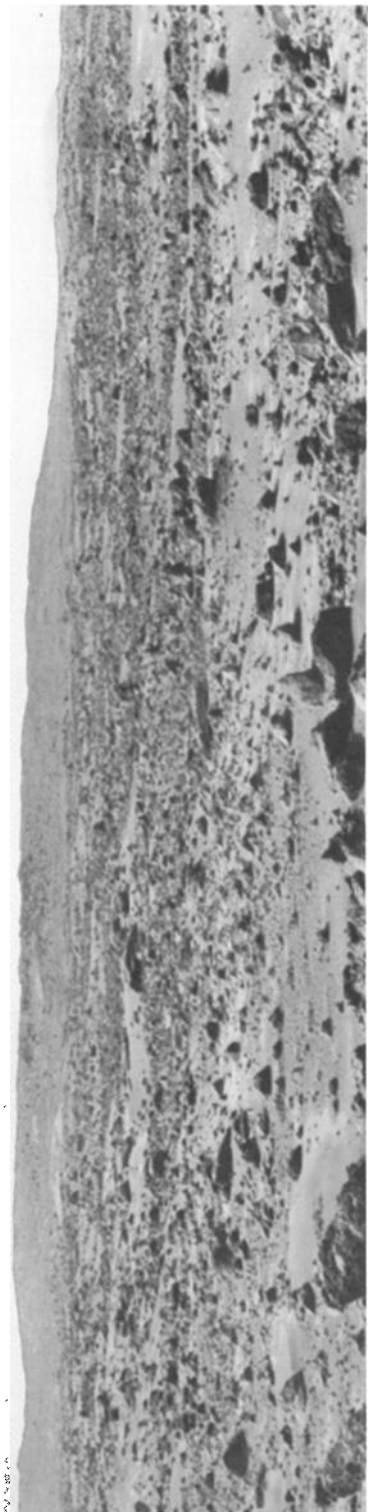


**Figure 5.** Manual super resolution panorama of Big Crater, about 2.2 km south-southeast of the lander, with Rimshot Crater visible on the lander facing rim of Big Crater (bright patch on center of rim). Note Far Knob to the right (south) and Southeast Knob to the left of Big Crater. See Figure 4 for orbiter views of these features. Cropped from five-frame mosaic of super panorama images processed to discriminate features at the subpixel scale.

projecting above the horizon, it lies on the outer northwest rim of Big Crater (Figure 5). This has also enabled viewing partway into the crater interior.

Because the lander came to rest on the southeast-facing flank of a gentle, broad ridge trending to the northeast (Figure 4), very distant features can be seen in the south and east directions, whereas relatively nearby features to the north, visible in the Viking Orbiter mosaic, are partially or completely obscured by the ground. Only the tip of North Knob projects above the local horizon, in spite of the fact that it appears to be a much larger feature than the Twin Peaks in the Viking Orbiter images. Similarly, a 300 m diameter crater, only 1.2 km to the northeast of the landing site, is completely obscured by the higher horizon to the northeast (Figure 4). Placement of the landing site is probably accurate to within about 100 m, with uncertainties due to correlating the azimuth directions outlined above in the ~40 m/pixel Viking Orbiter images. The Viking images were orthographically projected from off-nadir spacecraft viewpoints, with no knowledge of the local topography, so radial displacement of elevated features introduces a small error. Similarly, our ability to correlate small features at the surface with the Viking Orbiter views, such as peaks and rim crests, is subject to their sharpness on the ground and is limited by the ~40 m/pixel size of the Viking images.

The location of the Pathfinder lander in inertial space is provided by two-way ranging and Doppler tracking results, which indicate that the lander is at  $19.28^{\circ}\text{N}$ ,  $33.52^{\circ}\text{W}$  [Folkner et al., 1997b]. The determination of the location of the lander with respect to surface features to within 100 m and in inertial space to <100 m makes the Pathfinder lander the best located point on the surface of Mars. Ideally, the location in inertial space and with respect to surface features in a cartographic network should be the same. However, the position of the lander with respect to surface features in the USGS cartographic network [e.g., Howington-Kraus et al., 1995] differs by about 18.15 km to the west and 8.78 km to the north (Plate 2) from its inertial location, suggesting large errors in the network. A cartographic network for the local area [Duxbury, 1995] prepared from Viking stereo images, their pointing data, and revised orbiter positions places the lander at  $19.33^{\circ}\text{N}$ ,  $33.55^{\circ}\text{W}$  and suggests a similar offset (19.82 km to the east and 11.54 km to the south with respect to the USGS network). The offset between the position of the lander with respect to cartographic features in the local network of Duxbury [1995] and the inertial position of Folkner et al. [1997b] is 3.17 km. If the lander cartographic and inertial locations are the same, the local network has shifted too far to the south by 2.76 km and too far to the east by 1.67 km with respect to the USGS network (Plate 2). A more rigorous analysis of the exact location of the lander places it within one pixel in the Viking orbiter images (about 40 m) [Oberst et al., this issue], and a new control network using this position removes the severe offsets between the cartographic and inertial locations of features on Mars [Zeitler and Oberst, this issue].

#### 4. Heat Shield and Backshell Locations

Within view of the IMP camera are two anomalously bright spots, most notable in blue- and green-filtered images, that appear to be more than a kilometer from the lander. The first of these (Figure 8) was discovered during operations in a blue-filter super resolution frame (25 individual blue frames co-added) of the northern (left) side of the rim of Big Crater. It is

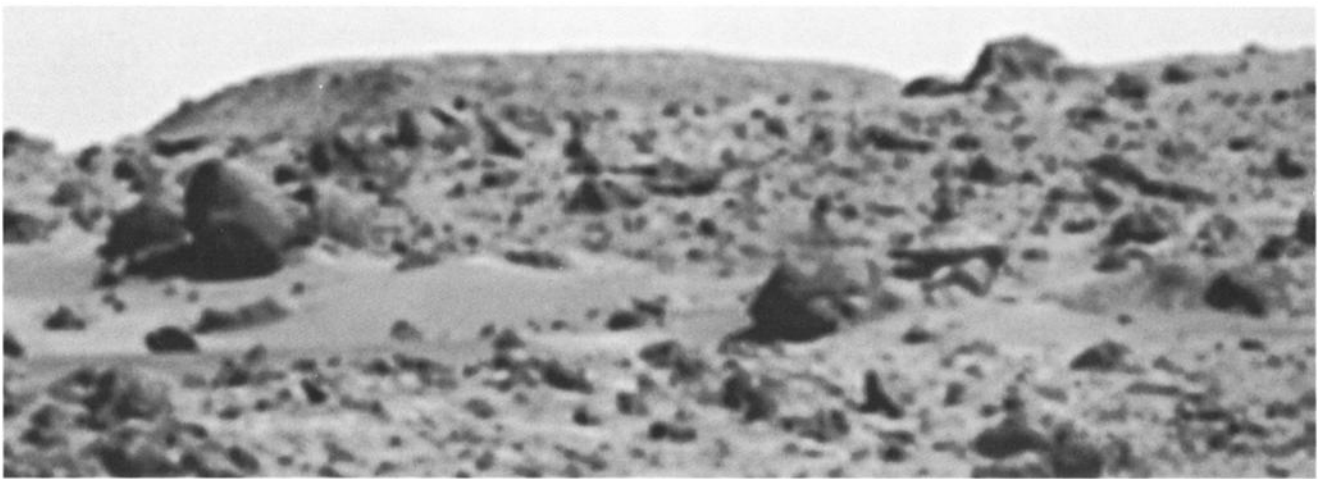


**Figure 6.** Portion of manual super resolution frame showing the summit of North Knob protruding above the relatively nearby northern horizon. North Knob lies about 1.7 km north of the lander. It subtends only  $7^\circ$  of azimuth from the lander perspective, but its base should subtend  $22^\circ$  from where the lander is in the Viking Orbiter images, confirming that much of it is hidden from view. Cropped from a single super panorama frame processed to discriminate features at the subpixel scale.

expressed as a spot subtending two or three pixels in an individual frame that is much brighter than anything in the scene, including the sky. It lies at an azimuth of  $137^\circ$  and an elevation of about  $2^\circ$  below horizontal. This bright spot could be outside of the spacecraft's conical backshell, which, because of its white color, would be bright in all wavelengths, but would stand out against the otherwise dark background in the blue. This bright spot was quickly identified in the previously acquired monster, gallery, and insurance panoramas (see later discussion of the various panoramas returned by the IMP). It was subsequently also recognized in the super panorama as well. Based on stereo parallax measurements (just under one pixel), it is estimated to be over a kilometer from the lander. Its brightness in all of these panoramas indicates it is lying on its

side with the apex of the cone pointed toward the lander, which is the side it would be expected to come to rest on from dynamical considerations during landing. The parachute, which is a light bluish/gray white color, cannot be separately identified; it could be draped over the backshell, or it could be lying on the ground.

The second bright spot (Figure 9) was identified near the horizon to the southwest of the lander in the super panorama (there is no super resolution image of this object). This feature is just below the horizon at an azimuth of  $208^\circ$  and an elevation of  $0^\circ$ . The spot is noticeably brighter than anything else in the far field in the blue filter images, with the exception of the sky, and glints off rocks in the Rock Garden (in the near and mid fields). This anomaly never subtends more than one

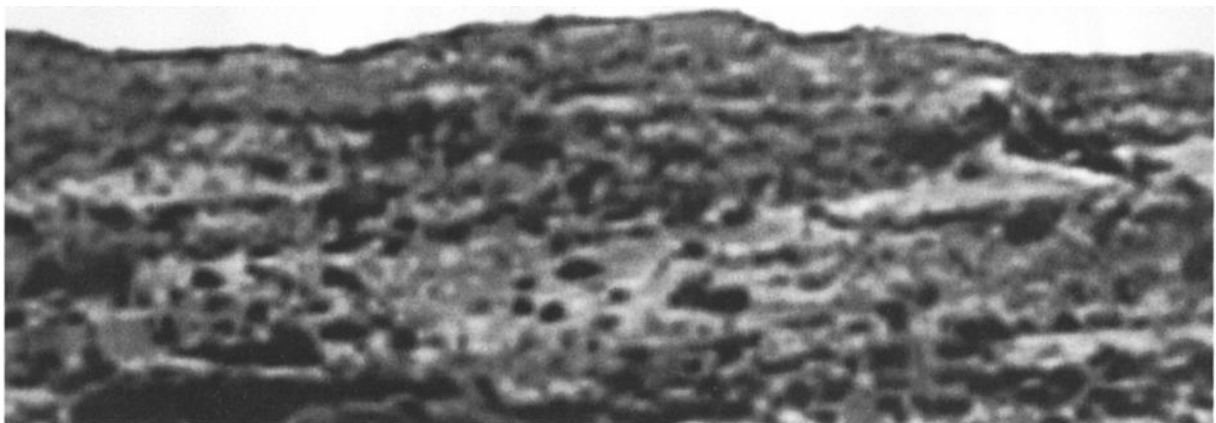


**Figure 7.** Portion of manual super resolution frame showing Little Crater to the east-southeast of the lander. This crater is of order 100 m in diameter and 1.2 km from the spacecraft. Cropped from a single super panorama frame processed to discriminate features at the subpixel scale.

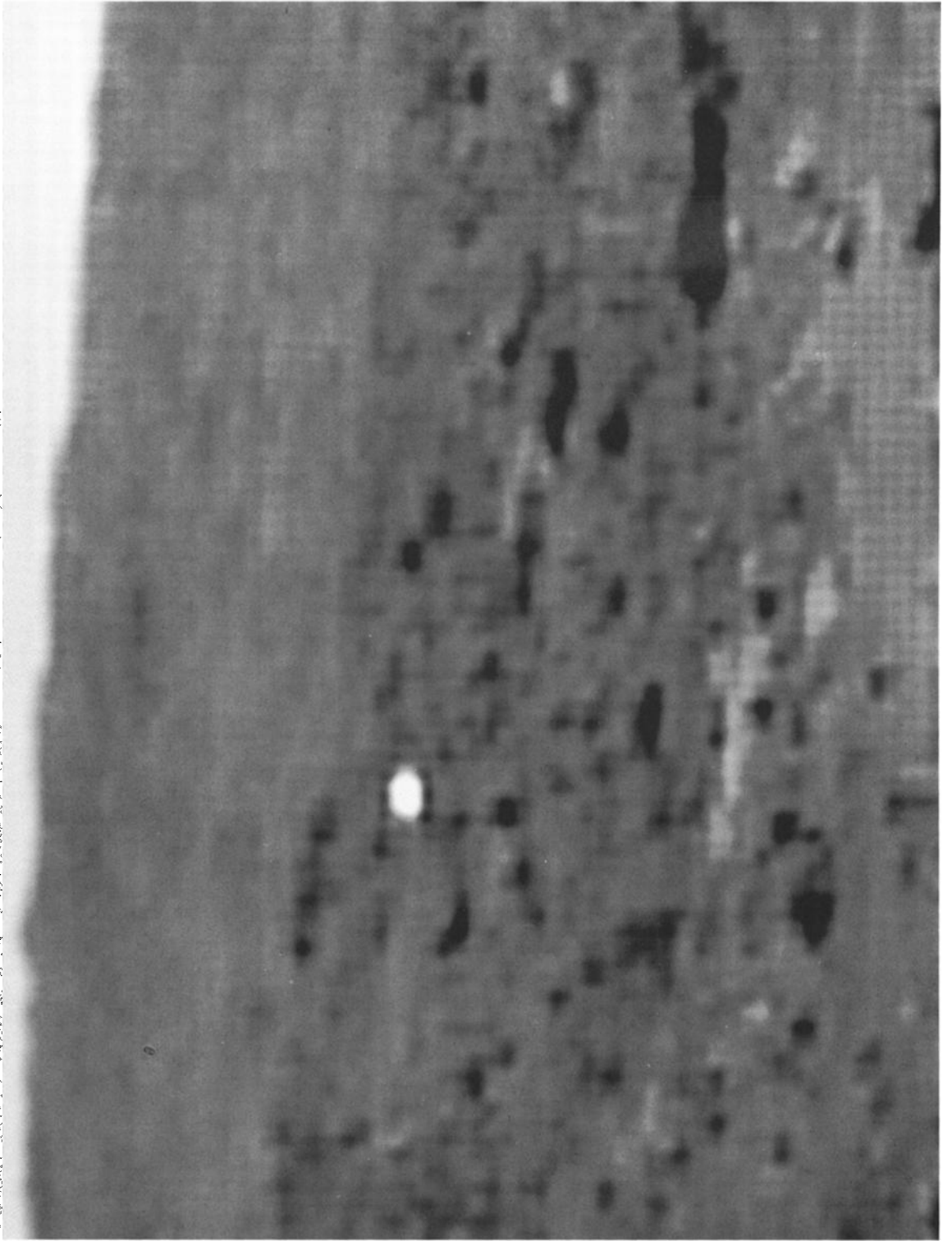


**Figure 8.** Super resolution blue-filter frame of the northern (left) edge of Big Crater and the terrain in the foreground, in which an anomalously bright spot was first identified (azimuth of  $137^\circ$ ,  $2^\circ$  below horizontal). This spot, covering two or three pixels, is brighter in the blue and green filters than anything else in the scene, including the sky, and may be the white outside of the spacecraft's backshell, jettisoned uprange and to the southeast of where the lander vehicle came to rest. The bluish/grayish white parachute cannot be separately resolved, but it could be draped over the backshell or be on the ground. This spot is about 1.2 km from the lander. Cropped from a single super resolution frame comprised of 25 repeat blue-filter frames acquired specifically for super resolution processing [Stoker *et al.*, this issue].

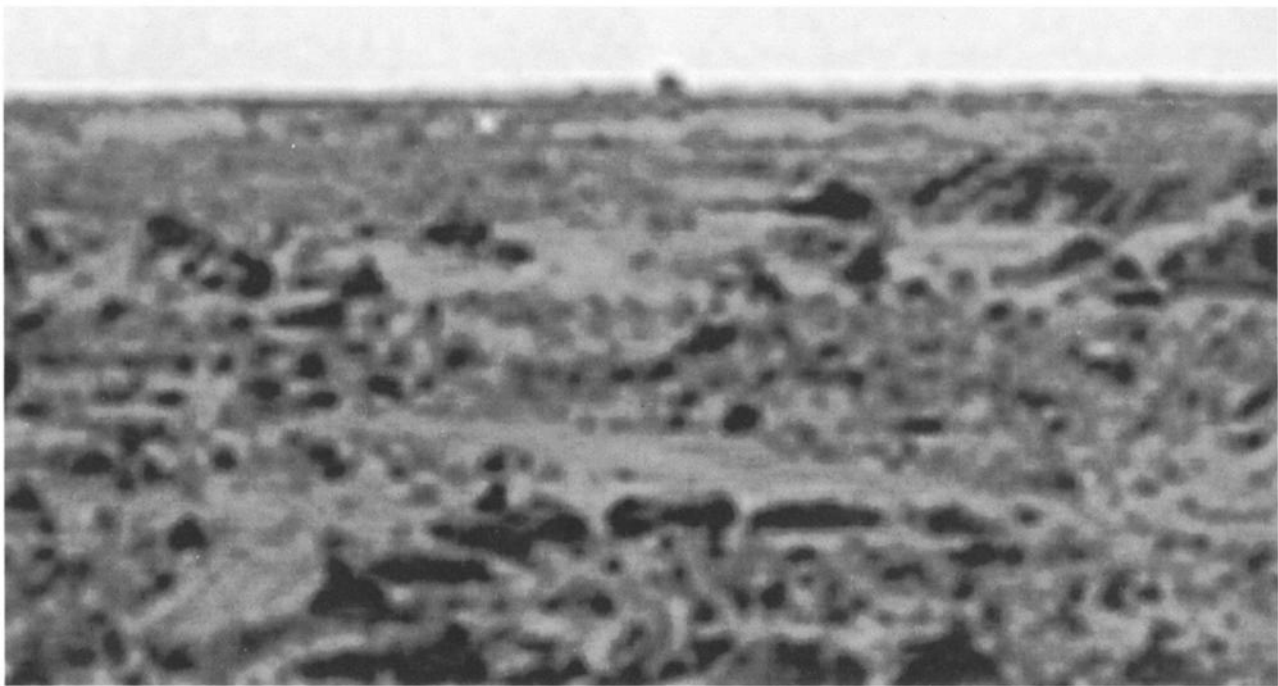


**Figure 9.** Portion of manual super resolution frame showing a second anomalously bright spot (in center of image, just below the horizon) to the southwest of the lander (azimuth of  $208^\circ$ ,  $0^\circ$  elevation). This spot is only one pixel or less in size but, like the first spot, is brighter in the blue and green filters than the surrounding terrain, excluding the sky and glints off rocks near the lander. It may be the inside reflective surface of the heat shield, jettisoned after the parachute was deployed, but which should have traveled farther downrange (to the southwest) of the landing site. The distance to this spot is difficult to determine, but it is probably about 2 km from the lander. Cropped from a single super panorama frame processed to discriminate features at subpixel scale.

pixel, so it is possible that it is much brighter but has been "subdued" by averaging with surrounding terrain. This anomaly is also recognizable in the monster and gallery panoramas, despite their 6:1 compression ratios. The object does not show in the insurance panorama, however, which was acquired late in the local afternoon, and so it may have been in shadow. The favored explanation for this bright spot is that it is the inside reflective surface of the heat shield, as the outside ablation surface is black. It would be lying on its side with the apex of the cone pointed away from the lander. The distance to this bright spot is difficult to measure because of the sub-pixel parallax displacement, but it is likely well over a kilometer away (that part of the horizon is farther than the Twin Peaks, which are about 1 km away).

Analysis of the telemetry from the landing as well as dynamical considerations of the landing scenario discussed earlier suggests that the heat shield should have gone downrange (toward the west-southwest) from the lander but that the backshell should have come to rest uprange (east-northeast) of the lander. If the large bright spot is the backshell of the spacecraft and the small bright spot is the heat shield, a line between the two would roughly describe the descent trajectory from east-northeast to west-southwest, plus or minus deflection of the backshell to one side or the other after the solid rockets fired (Figures 3 and 4). The lander would be expected to come to rest north of the line between the two if winds blowing toward the northwest and wind shear induced oscillations of the parachute, backshell, lander stack, implied by the landing recon-

struction (see earlier discussion), imparted a net velocity to the lander toward the northwest when the solid rockets fired, which also happened to be downhill. Figure 4 shows that the locations of the lander, heat shield, and backshell are as expected and in agreement with this landing reconstruction.

## 5. Air Bag Retraction and Surface Bounce Marks

Soil surfaces in the vicinity of the Mars Pathfinder lander that were clearly disturbed during the retraction of the air bags tend to appear darker than the surrounding undisturbed soils (Plates 4 and 5). Air-bag-retraction marks are evident as shallow trenches radial to the lander with pebbles and small rocks entrained in the soil nearest the lander. Similarly, rover tracks also appear darker than the surrounding surface. This darkening appears to indicate that the substrate beneath a very thin, relatively bright surface layer (likely atmospheric dust) is dark or that roughening of the soil surface reduces its reflectivity.

Patches of "darkened" soil, most too far from the lander to be attributable to air bag retraction, can be seen up to 15 m away from the lander to the east, and an arc of disturbed soil and rocks can be seen southwest of the lander [Golombek et al., 1997b]. Those to the southwest (Plate 5) lie roughly along an arc centered on the rover petal, between  $210^\circ$  and  $270^\circ$  azimuth (azimuths can be determined in Plate 6). The arc appears superposed on some rocks in the Rock Garden nearest to the

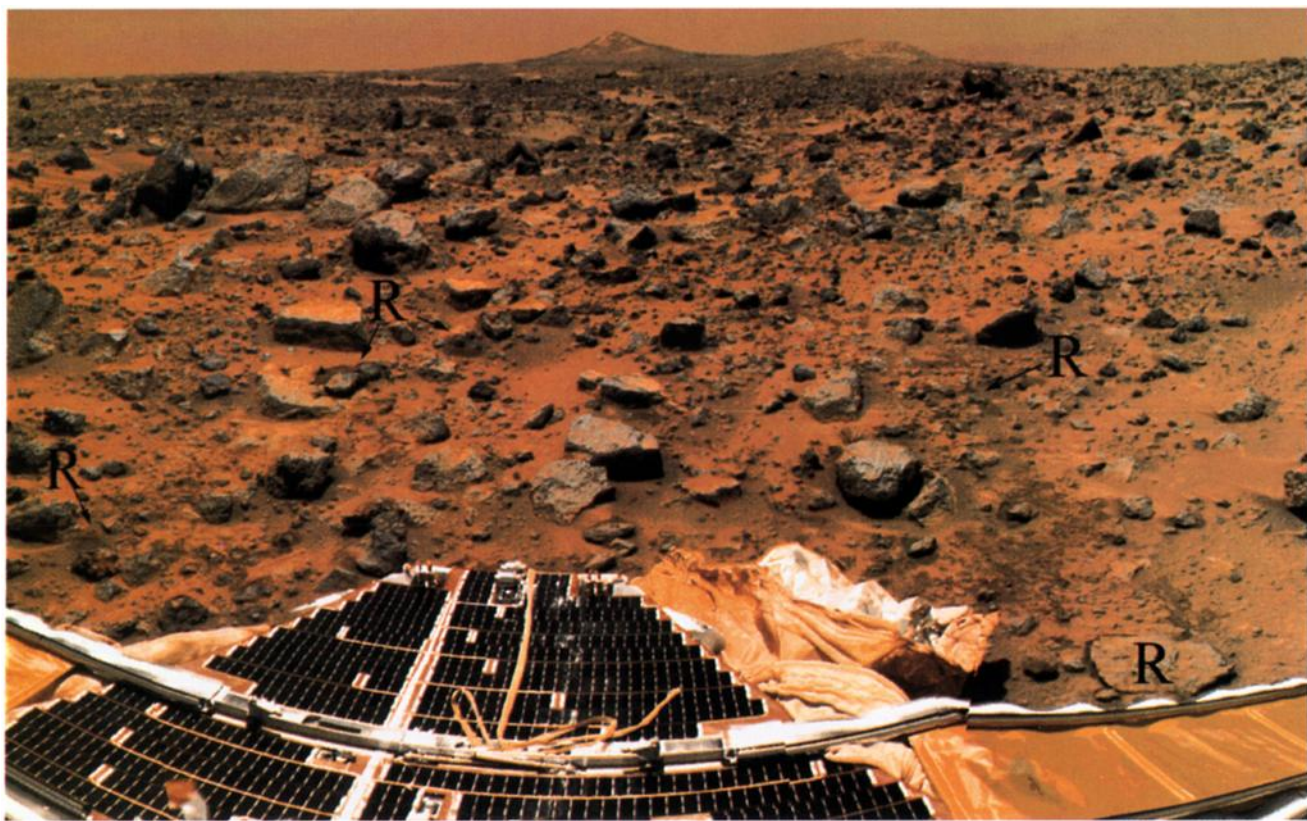


**Plate 5.** Additional disturbed soil surfaces to the southwest of the lander, defining an arc centered on the rover petal. The arc is expressed as darkened patches of soil and displaced rocks (labeled R) in the foreground of the Rock Garden. The air-bag-encased lander appears to have rolled gently up and back down the slight rise into the Rock Garden. Note Twin Peaks on the horizon. Image cropped from the gallery panorama.

lander. This arc appears to indicate that the air-bag-enclosed lander bounced from the east, then rolled gently up and back down the slight rise into the Rock Garden. The dark patches extending away from the lander to the east (Plate 4) are probably the spacecraft's last few bounce marks produced as the lander bounced to its present location from the east or east-southeast ( $90^\circ$  to  $130^\circ$  azimuth) after separating from the backshell and parachute. These marks differ from the roll marks and air-bag-retraction marks in that they are separate patches rather than continuous swaths. Those closest to the lander ( $70^\circ$  azimuth,  $35^\circ$  below horizontal) also show sharp, linear troughs that fade toward the edge of the disturbed patch. These appear to be impressions of creases in the air bags that were imprinted into the soil as the lander bounced, compressing the air bag lobe in contact with the ground.

## 6. Surface Operations

### 6.1. Team Structure

Mars Pathfinder employed subsystem, flight engineering, and experiment operations teams for spacecraft operations. The subsystem teams (power and pyrotechnic, propulsion, thermal control, flight software, attitude control, telecommunications, and navigation) were responsible for assessing the performance of and planning the future use of specific systems and subsystems on the spacecraft as well as on the ground. The flight engineering team assessed overall mission status; coor-

dinated the development of plans, sequences, and procedures; and validated planned activities in the flight system test bed and carried out real-time operations.

The experiment operations team was responsible for planning and conducting science activities and rover investigations. This team included the ASI/MET, IMP, and APXS instrument teams that were primarily responsible for planning the specific activities for each of their respective instruments. The rover operations team was responsible for planning and assessing the day to day rover operations activities as well as incorporating APXS and imaging science requests into the rover plan (a rover scientist and assistant rover scientist provided scientific guidance for rover activities). In addition to these teams, an additional part of the experiments operations team was seven science operations groups (SOGs) that were formed to address the operations needs of the interdisciplinary scientific investigations enabled by the combination of data from the rover, instruments, and engineering subsystems. All scientists associated with the mission (principal investigators, co-investigators, facility instrument science team members, participating scientists, and their associates) were part of a SOG. Table 1 shows scientists selected to be on the three instrument teams and the technology experimenters on the rover team; Table 2 shows the different science operations groups that were formed, their functions, and their membership (scientists are identified by their role in the project and their home institution). These SOGs were responsible for request-

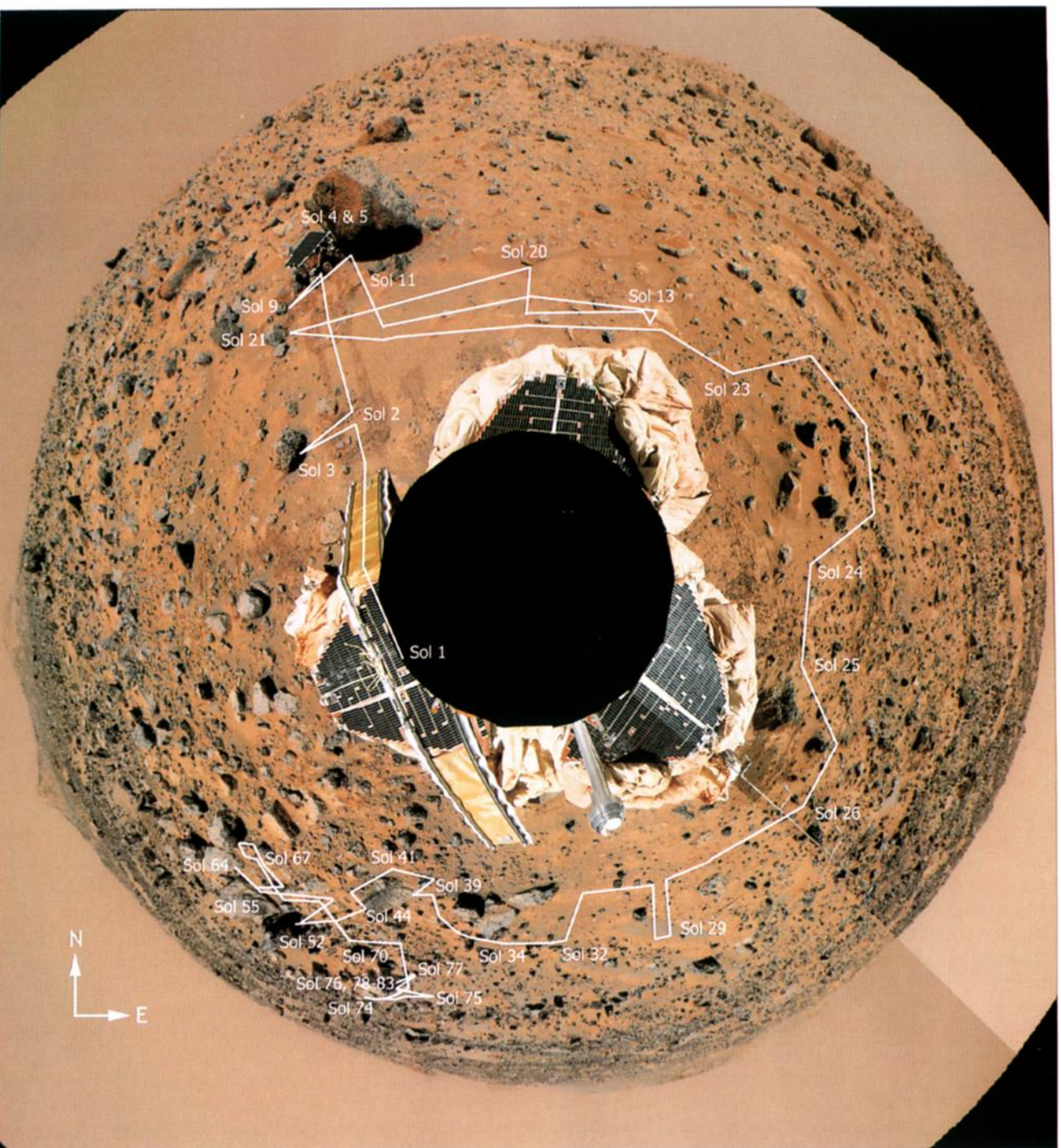


**Plate 6.** Azimuth-elevation projection (looking down at the center and progressively toward the horizon with distance from the lander) of the gallery panorama of the landing site with the rover traverse shown in white. Rover is adjacent to Yogi in the mosaic. Sols marked are from the end of day images of the rover. North is toward the top, with azimuths ( $0^\circ$ - $360^\circ$ ) mentioned in the text increasing in a clockwise direction.

ing measurements by the instruments, rover, and engineering subsystems for carrying out their scientific investigations and for analyzing the data and reporting on their findings.

## 6.2. Operations Scheduling

The Mars Pathfinder lander and rover are solar powered, so that most important surface operations such as rover traverses and downlink to Earth were carried out during Martian day-

light. Given that the Mars sol is 37 min longer than the Earth day, operations activities shifted relative to normal Pacific Daylight Time working hours at the Jet Propulsion Laboratory (JPL), where all mission operations were conducted. All operations planning and approval activities occurred during the Martian late afternoon, night, and early morning. Real-time operations activities occurred during the local Mars morning and daytime. During the nominal mission, three shifts worked

**Table 1.** Mars Pathfinder Instruments and Investigators

Description	Investigator	Position
<i>Imager for Mars Pathfinder (IMP)</i> A stereo imaging system with color capability provided by 24 selectable filters for the two camera channels. IMP also includes a magnetic properties investigation, the observation of wind direction and speed at three heights using small wind socks, and calibration, color, and reference targets mounted to the lander and rover.	P. Smith/U. Arizona D. Britt/U. Arizona L. Doose/U. Arizona F. Gleim/U. Braunschweig R. Greeley/Arizona State U. H. U. Keller/MPAE J. M. Knudsen/NBI R. Singer/U. Arizona L. Soderblom/USGS M. Tomasko/U. Arizona K. Herkenhoff/JPL	PI Co-I Co-I Co-I Co-I Co-I Co-I Co-I Co-I Co-I IS
<i>Alpha Proton Xray Spectrometer (APXS)</i> Alpha particle sources and detectors for back-scattered alpha particles, protons, and Xrays for determining elemental chemistry of surface materials.	R. Rieder/MPIC T. Economou/U. Chicago H. Wanke/MPIC J. Crisp/JPL	PI Co-I Co-I IS, ARS
<i>Atmospheric Structure Instrument/Meteorology Package (ASI/MET)</i> A set of accelerometers, temperature, pressure, and wind sensors mounted on the lander, providing entry and descent profile of atmospheric density, temperature, and pressure and regular meteorology monitoring.	J. T. Schofield/JPL J. Barnes/Oregon State U. D. Crisp/JPL J. Magalhães/ARC J. Murphy/ARC G. Wilson/Arizona State U.	TL, IS FIST FIST FIST FIST FIST
<i>Rover</i> Semi-autonomous vehicle for navigation, science investigations, and technology demonstrations Terrain geometry reconstruction/characterization Soil mechanics and sinkage Wheel abrasion  Material adherence Thermal characterization Dead reckoning and imaging sensor performance UHF link effectiveness	J. Matijevic/JPL H. Moore/USGS L. Mathies, B. Wilcox/JPL H. Eisen, D. Bickler/JPL D. Ferguson, J. Kolecki, S. Stevenson, D. Wilt/LeRC G. Landis, L. Oberle, P. Jenkins/LeRC H. Eisen, D. Braun, L.C. Wen/JPL A. Mishkin, H. Stone, A. Thompson/JPL L. Van Nieuwstad, H. Stone/JPL	TL RS TE TE TE TE TE TE TE
<i>RadioScience</i> Two-way radio system for precise measurement of lander position, rotation rate changes, precession rate, moment of inertia, orbital variations, and large asteroid masses.	W. Folkner/JPL	PS

See affiliation abbreviation and position descriptions in Table 2. TE, technology experimenters.

around the clock; each team worked during a particular period of the Martian day, which shifted forward about 24 hours during this time.

At the end of each sol, in preparation for the next sol, all of the subsystem specialists assessed the health and resources of the spacecraft and summarized data volume downlinked, problems or anomalies, necessary updates to power, thermal, and telecommunication models for mission planning software, and engineering activities needed for the next sol. One hour after the end of the last downlink of the day, scientists, through the SOGs and instrument teams, assessed what was learned and determined if changes were needed to the science plan for the next sol. Two hours after the end of the last downlink, the experiment operations planning group (EOPG) planned instrument and rover activities within the guidelines, constraints, and resource allocations for the next sol. Three hours after the end of the last downlink of the day, the long-term plan that contained the allotted Deep Space Network coverage and downlink opportunities was modified, and an engineering plan that contained all of the transmit sessions, battery charging commands, and other engineering and science activities was created that fit within the predicted thermal, power, and downlink constraints for the sol. Individual rover and science sequences were then developed that fit within the engineering and science plans. All sequences were reviewed and tested on an exact replica of the flight computer in a test bed at JPL to

validate that they would operate correctly on the spacecraft. Once the sequences were validated (sometimes this required an iteration with mission planners and sequence developers) and approved, they were uplinked to the spacecraft in the morning of the sol that they were executed, roughly 12 hours after the EOPG meeting (and the start of the next day's surface operations activities).

### 6.3. Surface Operations Activities

After receiving data indicating a healthy spacecraft at 1422 PDT on July 4 on the low-gain antenna, commands were sent to unlatch the IMP and high-gain antenna, and the imager was instructed to find the Sun. Using this information, the high-gain antenna was pointed toward Earth, and images were returned at 1630 PDT. Returned images included a panorama to determine how well the air bags had been retracted, stereo images of both ends of the rover petal to determine if it was safe to deploy the rover ramps, and a partial color panorama of the Martian surface and sky beyond the rover (Plate 3). These images indicated that the air bags would inhibit ramp deployment. As a result, the rover petal was lifted (closed) about 45°, the air bags were further retracted (five turns on the winch), and then the petal was lowered. Images returned at 2115 indicated that the air bags had been retracted enough to allow ramp deployment, which occurred at 2130, and the rover was com-

**Table 2.** Science Operations Groups (SOG), Objectives, Data, and Investigations, and Membership

SOG Investigations and Data	Members
Geology and geomorphology, eolian features, aerodynamic roughness, terrain geometry reconstruction. Data: IMP and rover images, wind sock data	<i>Geology and Geomorphology</i> M. Malin, MSSS, PS, SOG lead W. Ward, USGS, SOG lead R. Greeley, ASU, IMP Co-I H. U. Keller, MPAe, IMP Co-I R. Kirk, USGS A. Howington-Kraus, USGS L. Gaddis, USGS C. Stoker, ARC, PS R. Sullivan, ASU, PS R. Jaumann, DLR, PS L. Soderblom, USGS IMP Co-I T. Parker, JPL, Deputy SOG lead J. Oberst, DLR R. Kuzmin, Vernadsky Inst., PS A. Bennett, USGS M. Kraft, ASU J. Warren, MSSS E. M. Lee, USGS M. Sims, ARC R. Pischel, DLR
Mineralogy, petrology, and geochemistry Data: APXS data, IMP and rover images	<i>Mineralogy and Geochemistry</i> D. Britt, U. Arizona, IMP Co-I, SOG lead T. Economou, U. Chicago, APXS R. Rieder, MPIC, APXS PI, PSG J. Bell, Cornell U., PS J. Crisp, JPL, APXS IS, ARS S. Murchie, APL/JHU, PS H. McSween, U. Tennessee, PS H. Wänke, MPIC, APXS Co-I R. Singer, U. Arizona, IMP Co-I J. Johnson, USGS J. Greenwood, U. Tennessee R. Reid, U. Arizona R. Anderson, JPL N. Bridges, JPL T. Daley, Cornell U J. Brückner, MPIC A. Ghosh, U. Tennessee
Magnetism and mineralogy of airborne dust. Data: IMP images, APXS data	<i>Magnetic Properties</i> M. B. Madsen, NBI, SOG lead J. M. Knudsen, NBI, IMP Co-I R. Hargraves, Princeton U., PS A. Dinesen, NBI S. Hviid, NBI H. Gunnlaugsson, NBI W. Goetz, NBI C. Pedersen, NBI C. Mogensen, NBI
Physical properties of surface materials, abrasiveness. Data: IMP and rover images of tracks, rover engineering data	<i>Surface Materials Properties</i> H. Moore, USGS, PS, PSG, RS, SOG lead J. Crisp, JPL, ARS, APXS IS D. Bickler, JPL D. Ferguson, LeRC H. Eisen, JPL D. Wilt, LeRC J. C. Kolecki, LeRC J. Matijevic, JPL, Rover TL A. Haldemann, JPL E. Wellman, JPL J. Gensler, U. Texas K. Jewett, JPL
Atmospheric structure and meteorology. Data: entry and descent and surface data.	<i>Atmospheric Science</i> J. Barnes, Oregon St. U., ASI/MET FIST, SOG Lead T. Schofield, JPL, ASI/MET FIST TL, ASI/MET FIST D. Crisp, JPL, ASI/MET FIST G. Wilson, ASU, ASI/MET FIST J. Murphy, ARC, ASI/MET FIST A. Seiff, ARC, PS B. Haberle, ARC, PS S. Larsen, Riso Lab, PS L. Landberg, Riso Lab J. Magalhães, ARC, ASI/MET FIST
Aerosols, dust, clouds, and water vapor content Data: IMP images of the sky, material adherence.	<i>Atmospheric Imaging</i> N. Thomas, MPAe, SOG lead P. Smith, U. Arizona, IMP PI, PSG M. Tomasko, U. Arizona, IMP Co-I L. Doose, U. Arizona, IMP Co-I K. Herkenhoff, JPL, IMP IS M. Lemmon, U. Arizona P. Jenkins, S. Stevenson, LeRC D. Titov, IKI, PS G. Landis, LeRC J. Maki, U. Arizona R. Sablotny, MPAe E. Wegryn, U. Arizona
Precession rate, moment of inertia. Data: Two-way ranging and delay-Doppler tracking	<i>Rotational and Orbital Dynamics</i> B. Folkner, JPL, PS, PSG, SOG lead

PI, principal investigator; Co-I, co-investigator; PS, participating scientist; TL, team leader; FIST, facility instrument science team member; IS, investigation scientist; PSG, project science group member; RS, rover scientist; ARS, assistant rover scientist; JPL, Jet Propulsion Laboratory; USGS, U.S. Geological Survey; NBI, Niels Bohr Institute; ASU, Arizona State University; LeRC, Lewis Research Center; MPIC, Max Planck Institut für Chemie; MPAe, Max Planck Institut für Aeronomie; DLR-German Aerospace Center; ARC, Ames Research Center; MSSS, Malin Space Science Systems; APL/JHU, Applied Physics Laboratory/John Hopkins University, IKI, Space Research Institute.

manded to stand up. The meteorology mast was deployed at about 2030. A full panorama of the surface around the lander was returned during the last downlink of the first sol (sol 1 is July 4, sol 2 is July 5, and so on). The rover was driven down the rear ramp (the front ramp did not contact the ground) on sol 2 and acquired the first APXS measurement of soil that night. After the acquisition of an insurance panorama, the IMP was deployed on its 0.8 m high mast (not quite 2 m above the ground) at the end of sol 2. Following some communications difficulties between the rover and lander on sols 1 and 2, the rover placed the APXS against Barnacle Bill on sol 3 (see rock names in Figure 10).

Operations during the first week focused on returning a full stereo panorama (the monster panorama) to support rover operations and end-of-day images of the rover to allow traverse planning for the next sol (see later discussion of IMP opera-

tions). A full three-color gallery panorama was acquired on sol 10 and the super panorama (nearly lossless three-color stereo and nine other color filters) was begun on sol 13. This panorama and super resolution images represent the complete set of images for characterizing the landing site. The rover traversed in a clockwise direction around the lander to make APXS measurements of rocks in the Rock Garden, which could not be accessed from the other direction.

The lander battery degraded as expected during the first 30 days, so nighttime operations could only be conducted every 1-2 weeks after that time. Deep Space Network 70 m antenna coverage also decreased after the first 30 sols, which curtailed data return. The weeks following September 27, 1997, consisted of many failed and two successful attempts to communicate with the lander. The first successful transmission from the spacecraft during this period was on the auxiliary transmitter,

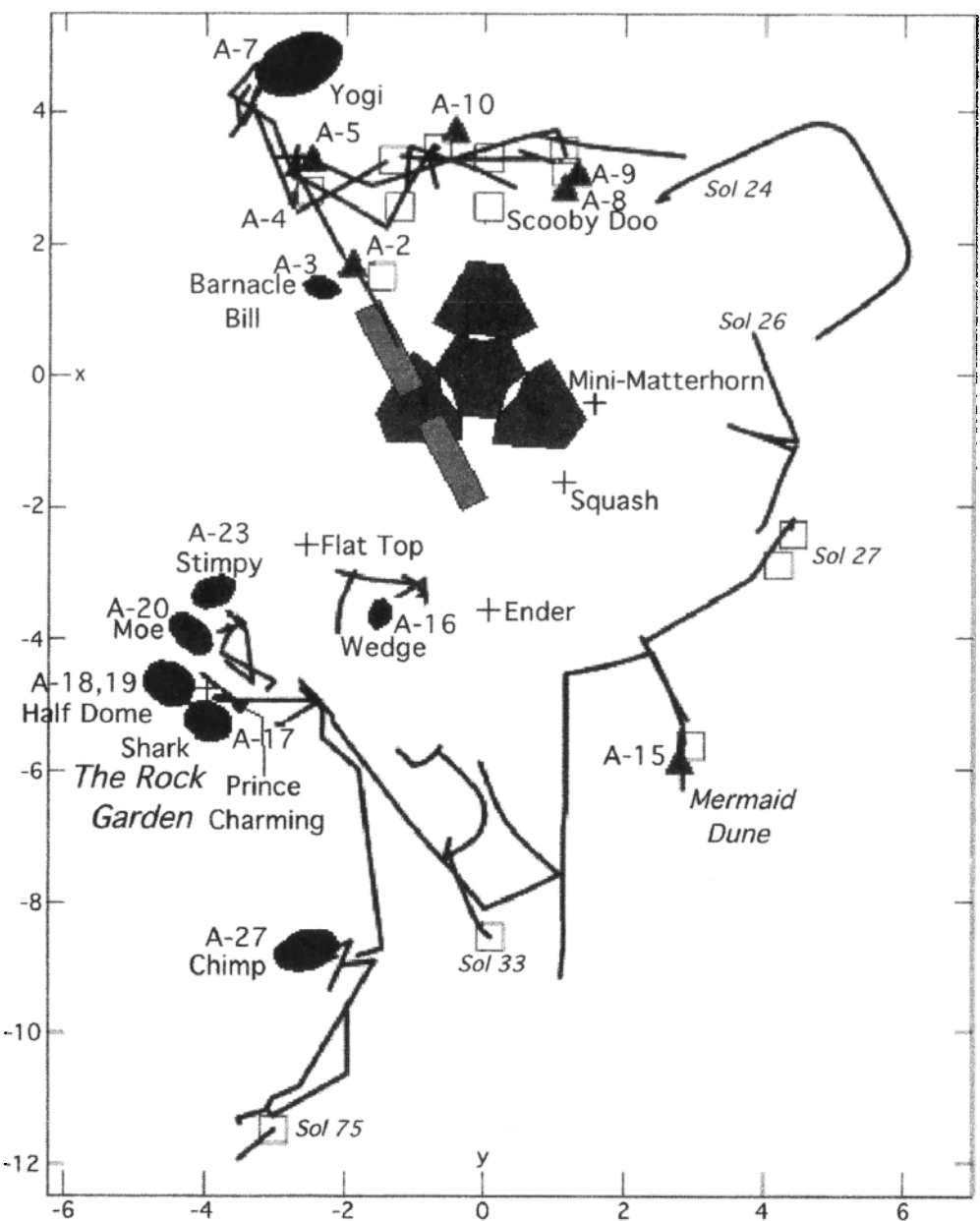


**Figure 10.** Map showing rover traverse and other activities at the landing site. In Mars local-level coordinate frame, the lander and rover ramps are shown schematically at the  $x=0$ ,  $y=0$  center point of the  $x$ ,  $y$  reference frame marked in meters (north is toward the top, in the plus  $x$  direction). Black lines show the rover traverse as a plot of the rover's estimated center positions. Gaps in curves are due to dead reckoning errors that built up during each drive. At the end of almost every day, the rover engineers reevaluated the rover position using IMP stereo images of the rover and uplinked a command to reset its position the next morning. The rover exited off the rear ramp toward the northwest and proceeded around the lander in a clockwise direction. Rocks with APXS measurements are shown as black ovals, with the rock name, and the APXS measurement number (A-2 to A-27). Soil APXS measurements are marked by black triangles with the APXS measurement number. Other rocks are noted by small crosses. Open boxes are locations of soil mechanics experiments. The location of the rover on beginning of some sols is marked (note differences with Plate 6, which reflects end of day locations). Daily rover operations can be found in Table 6, and APXS measurements can be found in Table 7.

and the second was believed to be on the low-gain antenna. The inoperable battery and the inability to operate the spacecraft resulted in the progressive cooling at night (with warming during the day) of the telecommunications hardware until, most likely, something in the telecommunications hardware broke due to thermal stress. The last communication with the spacecraft was on October 7, 1997. Attempts were made to

communicate with the spacecraft on a weekly to monthly basis until March 1998, but communications were not reestablished.

#### 6.4. Data Returned From Pathfinder

A summary of the volume of data downlinked from the Pathfinder spacecraft is shown in Table 3, categorized by application packet identification (APID). Each APID number identi-

**Table 3.** Downlink Data Volume: Total by APID

APID	Name	Bytes
1	Engineering, Housekeeping, and Accountability	3621329
2	Engineering, Housekeeping, and Accountability Recorded	4919947
3	Technology Image	2194038
4	Rover General Health and Status	516537
5	Rover Command Execution, Type 1	294478
6	Rover Sequence Execution Report	15168
7	Rover Critical State	50790
8	Rover Science Image	12289750
9	Rover Technology Image	3242231
10	Rover Lander Engineering Image	318236
11	Fault Notification	426
12	Alpha Proton Xray Data	562894
13	Technology, Rover Interface	
14	Time Correlation Packet	5685
15	Science Image, Type 1	17053242
16	IMP Error Packet	279040
17	Unrecognized Rover Packet	718131
18	Data Structures Packet	1916603
19	Science Image, Type 2	24488582
20	Operations Image, Type 1	7755252
21	Operations Image, Type 2	180495
22	Lander Engineering Image	38611
23	Rover Command Execution, Type 2	
24	Rover Image, Autonomous	714300
25	Rover Operations Image	12526927
26	Lander Image of Rover	4052747
27	Entry, Descent, Landing: Full ASI Dataset	95972
28	Flight Software Event Log: Fatal	583
29	Rover Traverse Command Execution	353718
30	Spare	
31	Entry, Descent, Landing: Critical Subset from EEPROM	4059
32	Atmospheric Study Image	12781784
33	Entry, Descent, Landing: Engineering from EEPROM	46635
34	Science Image, Type 3	83647688
35	ACS Engineering Packet	
36	IMP error Image	
37	MET Data	17729106
38	Entry, Descent, Landing: Science from EEPROM	22418
39	Entry, Descent, Landing: Full Engineering Dataset	68603
40	Science Image, Type 4	70630344
41	Flight Software Event Log: Warning	190502
42	Flight Software Event Log: Info	318111
Total Downlinked Data - Mission		287.5 Mbytes or 2.3 Gibits

APID, application packet identification.

fies a specific type of data. During the mission, each of these APIDs were prioritized such that the data that were most important at a particular time would have the highest priority to be downlinked to the ground. There are several imaging data APIDs to provide some imaging data a higher priority for downlink than other imaging data (i.e., rover navigation images had higher priority than super panorama data). By prioritizing these different APID queues, critical data were downlinked first and/or during the highest performance part of the telecommunications link. All mission operation plans and activities, uplink command sequences, and science (including some derived data products [Gaddis *et al.*, this issue; Kirk *et al.*, this issue]) and engineering telemetry data associated with Pathfinder have been documented (including calibrations [Reid *et al.*, this issue]) and archived into the Planetary Data System [LaVoie *et al.*, this issue].

### 6.5. IMP Operations and Data Returned

During the mission, the IMP returned 16,661 images. The largest number of images were taken of the sky and surface, followed by wind socks, the rover, astronomical targets, APXS sites, and magnetic targets, as shown in Table 4. Because the IMP could generate data at a much higher rate than could be

downlinked, various compression techniques, including lossy Joint Photographic-Experts Group (JPEG) compression, pixel averaging, and image subframing, were used, depending on the nature of the image data. The compression rates fell steadily after the first week of operations, and in most cases were lossless (1:3:1) or nearly lossless (2:1) by the end of the mission.

The first look (Plate 3) and pre-deploy panoramas were obtained on sol 1 to provide a color view of the surface and sky, assess the condition of the rover and any obstacles that might inhibit ramp deployment (in stereo), and assess the condition of the air bags (Table 5). They were fairly heavily compressed to allow their return on sol 1. A series of lossless insurance panoramas were obtained on the afternoon of sol 2 to guard against imager malfunction following deployment of its mast. All of these panoramas were taken before the mast was deployed at the end of sol 2. Although originally these panoramas were not expected to be returned, the data rates were high enough (downlink rates during the nominal mission were up to about 9 kbits/s into the 70 m antennas) to allow all of them to be returned during the first month of surface operations and before memory was lost when the computer was turned off at night. The stereo monster panorama was acquired on sol 3 to provide the information needed to plan rover traverses early in the mission and returned within the next couple of sols. A

**Table 4.** IMP Observation Summary

Observation (by Sequence)	Number of Images
Atmospheric (Sun and Sky)	4,832
Surface panoramas	3,774
Wind socks	1,812
Rover support	1,479
Astronomy	1,136
APXS sites, multispectral spots and slices	992
Magnetic targets	665
Super resolution	585
Radiometric calibration targets	567
Photometric spots	321
Miscellaneous (dust devil search, change monitoring, deep field test, Yogi photometry, fiducial marks)	252
Dark frames, dark/null strips	26 (cruise), 220
Total	26 (cruise) 16,635 (surface) <b>16,661 total images</b>

The number of images by observation sequence name, which controlled downlink allocation. Note that some observation sequences produced images that can be categorized into more than one group.

full-color gallery panorama was acquired and returned during the beginning of the second week of surface operations to provide a seamless full panorama in color. This was a five-tier, 6:1 JPEG compressed panorama (the previous pans were four tiers) in three filters (440 nm, 530 nm, and 670 nm), acquired over 3 days in a time continuous fashion (495 images total). The super panorama was acquired throughout the rest of the mission, with each segment optimized for lighting geometry. This panorama, of which 83% was completed before loss of the spacecraft, was lossless in the red and blue stereo filters and almost lossless (2:1) in all other filters. Many super resolution sequences were taken, in which multiple images of the same area were taken (typically in the blue filter) with slightly different pointing to allow resolutions below a pixel [Stoker *et al.*, this issue].

As a key part of rover operations, the IMP camera provided daily updates (end of day) on the location and status of the rover. These images are stereo images, typically JPEG compressed at 6:1, and acquired in the 670 nm filter. The rover

**Table 5.** IMP Panorama Table

Panorama	Description <sup>a</sup>	Number of Images	Horizontal Angular coverage, deg	Observation Time
First Look <sup>b</sup>	R440(12:1,2x2)=32 R670(24:1,1x1)=19 RL670(12:1,1x1)=26 R670(80:1,1x1)=15 R530(12:1,2x2)=32 R440(q=09,2x2)=07 R670(q=15,1x1)=07 R530(q=09,2x2)=07	145	140	sol 1 morning
Predeploy red/IR	R670(12:1,1x1)=30 R670(q=15,1x1)=20 R965(6:1,1x1)=89	139	red=220 IR=360	sol 1 morning
Insurance	RL440(los,1x1)=84 R530(los,1x1)=84 R600(los,1x1)=84 R750(los,1x1)=84	420	360	sol 2 morning
Monster	R440(6:1,2x2)=50 R530(6:1,2x2)=50 RL670(6:1,1x1)=195 R750(6:1,2x2)=50 R965(6:1,2x2)=50	395	360	sol 3 various
Gallery	R440(6:1,1x1)=132 R440(q=65,1x1)=33 R530(6:1,1x1)=132 R530(q=65,1x1)=33 R670(6:1,1x1)=132 R670(q=65,1x1)=33	495	360	sol 9, 10, 11 morning
Super	RL440(los,1x1)=119 <sup>c</sup> R480(2:1,1x1)=119 R530(2:1,1x1)=119 R600(2:1,1x1)=119 RL670(los,1x1)=119 R750(2:1,1x1)=119 L800(2:1,1x1)=119 L860(2:1,1x1)=119 L900(2:1,1x1)=119 R930(2:1,1x1)=119 RL965(2:1,1x1)=119 L1000(2:1,1x1)=119	1785 <sup>d</sup>	360	various

<sup>a</sup>Key: exxx(comp,pa)=n, where e is (R)ight or (L)eft eye, xxx is wavelength (nm), comp is compression ratio, pa is pixel averaging size, and n is number of images (q is quality factor) and los is lossless compression (Rice). Camera is in the predeployed state for observations made before sol 3.

<sup>b</sup>Also called mission success panorama.

<sup>c</sup>Compression in RL440 began as 2:1 JPEG and was later changed to lossless during acquisition.

<sup>d</sup>Includes only complete cubes.

team used these images to determine the position of the rover after traverses, turns, and wheel movements. The IMP was also used with the rover for soil mechanics experiments, rover track imaging, and rover dust accumulation monitoring (on the wheels and on the solar panel). The IMP also acquired time lapse images of the rover as it drove across the Martian surface (i.e., a "rover movie"), which provided additional documentation of rover activities. The rover movies were JPEG compressed at 24:1, the frames were typically spaced 15 s apart in time and were approximately 15–25 frames in length.

### 6.6 Rover and APXS Operations and Data Sets

The rover traversed a total of 104 m around the lander in a clockwise direction staying within 12 m of the lander (Plate 6 and Figure 10). It traveled using 212 directed or commanded movements (move a prescribed distance, turn to a particular heading), 20 higher level waypoint commands (move to a particular x, y location), and two high-level commands to find rocks (move to a particular x, y location and use laser light stripers to place vehicle in front of rock). It returned a total of 564 black and white, stereo, and color images. It performed about 10 technology experiments (see Table 1) that included special sensors to measure adherence of dust to the solar panel (148 material adherence experiment measurements) and the abrasiveness of soils (11 wheel abrasion experiment measurements) (see *Rover Team* [1997b] for a description of these experiments). "In honor of an outstanding contribution to planetary geology, as the first mobile geological rover on Mars," Sojourner was made an honorary Fellow of the Planetary Geology Division of the Geological Society of America at the annual meeting in October 1997.

Rover operations planning was done on three timescales: long, intermediate, and short term. Long-term planning looked 1 to 3 months ahead every 3 weeks or so to derive a list of rover activities to be undertaken in sequential order. Intermediate planning was done once a week, to plan the next week's rover activities. Here the level of detail included the planned rover traverse, the data volume for each image and each sol (to be sure it meshed with the overall engineering schedule and downlink forecast), what each image would contain, and experiments planned for each particular day. Short-term planning, such as commanding of particular APXS measurements, imaging, soil mechanics experiments, and specific driving commands reacted in near-real time to the previous day's events and the latest science discoveries. Difficulties deploying the APXS to a particular location, driving over rough terrain, or communicating between Earth and Mars often resulted in a slip in schedule.

In the operations planning, a balance was maintained between APXS measurements, soil mechanics experiments, imaging, and technology experiments. A high priority was given to taking APXS measurements of a diversity of rock types (preferably the least oxidized ones) and soil types and documenting them with front rover camera images and an image from the rear rover camera showing the APXS deployed to the sample. Soil mechanics experiments performed with the rover wheels and close-up imaging before and after were used to characterize the different soil types and any variations in soil properties with depth. The APXS measurements were usually done in afternoon and at night, allowing time in the morning or during traverses for other rover experiments.

Rover position data from telemetry are plotted as a traverse path in Figure 10. A summary of rover activities, with the rover's position at the beginning of each sol is given in Table 6. The rover nearly circumnavigated the lander (clockwise). The early phase of the mission took place to the north of the lander, where several soil mechanics experiments were done in the areas clear of rocks. Early APXS analyses were taken of rocks (Barnacle Bill and Yogi) and a variety of soils near the end of the ramp and to the east (cloddy deposits between the ramp and Yogi, Scooby Doo, wheel-disturbed soil next to Scooby Doo, and soil next to Lamb). Soil mechanics experiments were done in a variety of cloddy materials (S-1, 2, 3, 4, 6, 8). A soil mechanics test (S-5) of Scooby Doo failed to scratch it, and an area of highly compressible fine-grained dust was discovered in a wheel-spinning test next to Casper (S-9). A "null zone" for modem communication between lander and rover behind Yogi prevented any driving in that area.

The high sulfur content of the rock analyses indicated that the APXS may have sampled only weathered rock or rock covered by a sulfur-rich dust or soil, so a decision was made to drive toward the Rock Garden for more rock APXS analyses. This is an area to the southwest of the lander containing several large rocks (Plates 3 and 6), some of which have low red/blue ratios and what appeared to be steep faces. A trafficability analysis by the rover engineers indicated that the rover would have to take the long route clockwise around the lander to get to the Rock Garden, to access this area. On the way, soil mechanics experiments were done in some layered deposits of mixed cloddy and drift materials in areas clear of rocks southeast of the lander (S-10, 11). Soil mechanics (S-12) and APXS tests were run on Mermaid Dune. Two additional soil mechanics tests were performed just outside the Rock Garden (S-13, 14). The Rock Garden terrain was difficult for rover driving, and the loss of the rover battery on sol 56 slowed down operations, but during the last 46 sols, seven additional rock APXS analyses were obtained. The APXS was deployed to steep faces on Shark and Chimp; Shark had the lowest red/blue ratio of all the chemical measurements and the highest silicon content. Soil mechanics tests were not done inside the Rock Garden because of the lack of clear areas of soil and the priority given to APXS measurements. A total of 25 soil mechanics experiments were performed.

Over the 83 sol mission, APXS measurements were obtained for eight rocks (two locations on Half Dome), six soil-like materials, and one indurated soil or rock (Scooby Doo), as summarized in Table 7. Measurements of the atmosphere were obtained on sol 1 for background cosmic ray calibration and briefly on sols 10, 24, and 25 for electronics noise tests. When the APXS failed to deploy to the desired rock targets on sols 22, 66, 67, 76, 77, and 78, measurements of the atmosphere were also made, and these serve as additional background calibrations. When measuring rock and soil samples, the desire was to obtain at least 10 integrated hours for the alpha and proton modes, although only 3 hours of nighttime measurement was needed for an X-ray analysis (daytime spectra were noisy). Shorter measurement times provide useful, albeit noisier results. Actual spectral accumulation times for the rock and soil analyses ranged from 5 to 16 hours. After the rover battery died on sol 56, the APXS data was noisier (especially for sodium). Good contact was made with the APXS deployment mechanism for all samples except A-2 and A-9.

**Table 6.** Summary of Rover Operations, Images, APXS Analyses (A-), Soil Mechanics Experiments (S-), Technology Experiments (T-), and Wheel Abrasion Experiments (W-)

Sol	Rover Activities
1	Landing, APXS background (A-1)
2	SVP X=-0.444, Y=-0.869, H=155.00; ramp deployment, rover deployment, egress, APXS deploy (A-2) (X=1.89, Y=-1.95, Z = 0.31)
3	SVP X=1.587, Y=-1.784, H=150.99; RC image of APXS site; soil mechanics experiment using LF wheel, reverse 1/4 turn (S-1) (X=1.49, Y=-1.49, Z=0.37); RF compressed image of tracks and lander; place APXS on Barnacle Bill (A-3) (X=1.30, Y=-2.45, Z=0.18)
4	SVP X=1.515, Y=-1.980, H=68.42; retract APXS; wheel abrasion experiment 2 spins (W-1) X=1.41, Y=-1.71, X=0.034); rover operations no load current, LF wheel; pop a wheelie (T-1) (X=1.76, Y=-1.81, Z=0.34); soil mechanics using RR and right front wheels 3/4 turn (S-2) (X=2.79, Y=-2.52, Z=0.28); wheel abrasion experiment, 7 spins (W-2) (X=3.26, Y =-2.45, Z=0.24); LF and RF mapping images of Yogi base; APXS deployment (A-4) (X=2.79, Y=-2.64, Z=0.28)
5	SVP X=3.277, Y=-2.690, H=6.82; APXS retract; RC images of APXS site (A-4); wheel abrasion experiment, 7 spins (W-3) (X=3.26, Y =-2.45, Z=0.24); LF and RF images of Yogi, tracks, and wheel trench; LF and RF images of lander, tracks, and backsides of rocks; APXS deploy (A- 5) (X=3.29, Y=-2.48, Z ~ 0.28); RC images of APXS deployed
6	SVP X=2.990, Y=-2.745, H=188.27; RC image of Yogi; position APXS on Yogi; RC image of Yogi; LF and RF camera images of Cradle, tracks, and backsides of rocks
7	SVP X=4.341, Y=-3.278, H=201.00; RC image of APXS
8	SVP X=4.341, Y=-3.278, H=201.00; LF camera images of Cradle, tracks, and backsides of rocks; APXS deploy; RC image of Yogi; RC image of APXS site
9	No activities. No change in vehicle position.
10	SVP X=3.633, Y=-3.647, H=216.36; electronics noise test of APXS (A-6); position APXS on Yogi (A-7) (X=4.58, Y=-2.91, Z=-0.18); RC image of APXS site; LF and RF camera images of rocks and tracks to west
11	SVP X=4.335, Y=-3.242, H=205.25; end APXS read (A-7)
12	SVP X=4.335, Y=-3.242, H=205.25; wheel abrasion experiment, 7 spins (W-4) (X~2.67, Y~-1.14); LF and RF camera images of rocks to the east
13	SVP X=2.804, Y=-1.125, H=74.70; soil mechanics experiment using both wheels in cloddy sollike deposit (S-3) (X=3.26, Y= 1.33, Z=0.29); soil mechanics experiment using RR wheel on Cabbage Patch (S-4) (X=3.30, Y=0.04, Z=0.30); LF and RF camera images of Scooby Doo and Casper and mapping images of tailings of deposits of Cabbage Patch; RC image of Casper
14	SVP X=3.578, Y=0.384, H=255.00; wheel abrasion experiment, 7 spins (W-5) (X=3.58, Y=0.38); deploy APXS on Scooby Doo (A-8) (X=2.85, Y=1.13, Z=0.32); LF and RF camera images of Casper, Shaggy, and tracks; RC images of Scooby Doo; begin APXS readings on Scooby Doo (A-8)
15	SVP X=3.273, Y=1.028, H=337.76; RC images of Scooby Doo, soil mechanics experiment and test for crust or rock using 1/4 turn of RR wheel on Scooby Doo (S-5); strip surface of Scooby Doo and draw-bar pull (S-5) (X=3.08, Y=1.15, Z=0.28); RC images of Scooby Doo; deploy APXS on disturbed surface (A-9) (X=3.08, Y=1.32, Z=0.28); LF and RF camera images of Yogi
16	No downlink, no change in position
17	No activities, no change in position
18	SVP X=3.240, Y=0.955, H=294.00; retract APXS; soil mechanics experiment using LF wheel in Cabbage Patch, full reverse spin (S-6) (X=2.55, Y=0.04, Z=0.32); LF and RF camera mapping images of tailings of deposits of Cabbage Patch; soil mechanics experiment using LF wheel south of Yogi, full reverse spin (S-7) (X=2.55, Y=-1.23, Z=0.20); LF and RF camera mapping images of tailings of deposits south of Yogi; wheel abrasion experiment, 7 spins (W-6) (=2.92, Y= -0.85); RC image of APXS site
19	No change in position
20	SVP X=2.856, Y=-0.711, H=191.84; no load wheel current, left front wheel, one full turn on left center wheel (pop a wheelie, T-2) (X=2.54, Y=-0.56, Z=0.33); LF image of wheel; end no load wheel current (pop a wheelie); begin APXS deploy on soil near Lamb (A-10) (X=3.74, Y=-0.43, Z=0.28); RC image of APXS site
21	SVP X=3.452, Y=-0.692, H=299.00; retract APXS; soil mechanics, LR wheel, 1 1/2 turns (S-8) (X=3.45, Y=-0.69); no load wheel current, LF wheel, 3/4 turn on left center wheel (pop a wheelie T-3); LF camera image of LF wheel during test; LF and RF camera images toward Yogi; LF and RF camera images looking toward Souffle; LF and RF camera images looking toward Souffle; RC image of Souffle; Wheel abrasion experiment, 7 spins (W-7) (X=3.15, Y=-2.56)
22	SVP X=3.318, Y=-2.602, H=65.63; deploy APXS (A-11) (X~ 3.00, Y~3.60); RC image of deployed APXS; start APXS (A-11)
23	Retract APXS (APXS missed Souffle); soil mechanics, RF wheel, reverse, one turn (S-9) (X=3.42, Y=1.11, Z=0.23); LF and RF camera images of soil mechanics trench; LF and RF camera images along H=50.00; wheel abrasion experiment (W-8) (X=2.43, Y=2.74, Z=0.10)
24	SVP X=2.694, Y=2.603, H=71.50; LF and RF camera images to south; aborted soil mechanics; LF and RF camera images of surface detail; LF and RF camera images of lander; APXS noise tests (A-12,13,14)
25	SVP X=0.542, Y=3.750, H=270.00
26	SVP X=0.626, Y=3.837, H=46.0; LF and RF camera images of Mini-Matterhorn and lander; LF and RF camera images of Pooh Bear, Squash, Mermaid, "pebbly" surface, and drift
27	SVP X=-2.334, Y=4.386, H=197.00; LF camera image of LF wheel and poorly sorted deposit; soil mechanics experiment, RR wheel one-half turns forward (S-10) (X=-2.43, Y=4.42, Z=0.25); soil mechanics experiment, RR wheel one-half turns forward (S-11) (X=-2.89, Y=4.21, Z=0.31); LF and RF camera images of lander and Squash; RC image of Mermaid
28	SVP X=-5.423, Y=2.847, H=354.24; wheel abrasion experiment, RR wheel forward 0.3 turns, RF wheel backward 0.3 turns, and spin right center wheel (W-9)(and T-4) (X=-5.39, Y=2.94, Z~0.50); wheel abrasion, RR wheel backward 1.2 turns, RF wheel forward; deploy APXS to surface of Mermaid dune (A-15) (X=-5.87, Y=2.80, Z=0.52)
29	SVP X=-5.612, Y=2.847, H=358.20; begin APXS retraction; soil mechanics experiment, LR wheel forward one and one-half turns (S12) (X=-5.64, Y=2.55, Z=0.51); soil mechanics experiment, RF wheel backward one turn (S-12) (X=-5.65, Y=2.96, Z=0.52); soil mechanics experiment, LR wheel forward one and one-half turns (S12) (X=-6.17, Y=2.52, Z=0.54); LF and RF camera images of excavation in Mermaid dune; LF and RF camera images of lander, tracks, and Squash; LF and RF camera images of lander, Rover tracks and Squash
30	No change in vehicle position
31	No change in vehicle position
32	SVP X=-6.024, Y=2.778, H=4.90; LF and RF camera images of Squid and Hassock; LF and RF camera images of entrance to Bookshelf; soil mechanics Experiment, RR wheel, forward one and one-half turns (S-13) (X=-8.56, Y=0.09, Z=197.0);
33	SVP X=-8.562, Y=0.091, H=197.00; LF and RF camera images of lower rock garden; LF and RF camera images of Ender, Hassock, and lander
34	No activities, no change in vehicle position
35	SVP X=-5.907, Y=-0.062, H=341.22; LF and RF images of lander; LF and RF mosaic images of Wedge and Flat Top
36	SVP X=-3.498, Y=-0.885, H=91.95; LF and RF images of Ender, Chimp, and Snoopy; LF and RF mosaic images of Ender, Chimp, and Snoopy
37	SVP X=-3.448, Y=-0.837, H=178.30; deploy APXS; final APXS positioning (A-16) (X=-3.79, Y=-1.31, Z=0.12); RC mosaic image of APXS Wedge; LF and RF full mosaic images looking toward lander
38	No change in vehicle position
39	SVP X=-3.419, Y=-0.973, H=45.67; begin APXS retraction; wheel abrasion experiment; tare for right center wheel, wheelie (T-5), RR wheel forward 0.3 turns, front wheel backwards 0.3 turns, and spin right wheel (W-10); soil mechanics experiment; tare for RF wheel, pop-a-wheelie (T-6), right center wheel forward 0.75 turns, RF wheel forward 1.0 and backwards 1.0 turns, right center wheel backward 0.75 turns (X~3.35, Y~0.90)

**Table 6.** (continued)

Sol	Rover Activities
40	SVP X=-3.398, Y=-0.862, H=342.00; LF and RF mosaic images of entrance to rock garden; LF and RF mosaic images of Shark
41	SVP X=-3.398, Y=-0.862, H=342.00; LF camera image of Shark, Flat Top, and lander
42	SVP X=-3.166, Y=-1.033, H=301.04; LF and RF mosaic images of Flat Top and Stimpy; LF and RF mosaic images of Wedge and Hassock
43	SVP X=-2.996, Y=-1.858, H=149.36
44	No change in vehicle position
45	SVP X=-3.791, Y=-1.987, H=184.74
46	No change in vehicle position, no activities
47	SVP X=-3.696, Y=-1.955, H=184.00
48	No change in vehicle position, no activities
49	SVP X=-4.159, Y=-2.077, H=197.31; RC mosaic image lost; LF and RF camera mosaic images of Shark
50	No change in vehicle position
51	No uplink or downlink; no change in vehicle position
52	SVP X=-5.350, Y=-2.892, H=54.90; deploy APXS (A-17); RC mosaic of Shark; start APXS analysis of Shark (A-17) (X=-5.56, Y=-3.25, Z=-0.35)
53	SVP X=-3.398, Y=-0.862, H=342.00; retract APXS (A-17); wheel abrasion experiment (W-11) (and T-7) (X~-5.11, Y~-2.15); RC mosaic of Half Dome
54	SVP X=-4.934, Y=-3.718, H=93.17; turn and deploy APXS; RC mosaic of Half Dome; start 1st APXS analysis of Half Dome (A-18) (X=-4.81, Y=-3.81, Z=-0.54)
55	SVP X=-4.934, Y=-3.718, H=73.00; deploy APXS; RC mosaic of Half Dome; start 1st APXS analysis of Half Dome (A-18) (X=-4.81, Y=-3.81, Z=-0.54)
56	SVP X=-4.934, Y=-3.718, H=73.00; rover battery dies in early morning; retract APXS; deploy APXS; RC mosaic of Half Dome; start 2nd APXS analysis of Half Dome (A-19) (X=-4.82, Y=-4.13, Z=-0.59)
57	Vehicle position unchanged, no rover uplink
58	Vehicle position unchanged; continue 2nd APXS analysis of Half Dome (A-19)
59	Vehicle position unchanged, no rover downlink
60	Vehicle position unchanged; retracted APXS then deployed it to same location
61	Vehicle position unchanged
62	Vehicle position unchanged; continue 2nd APXS analysis of Half Dome (A-19)
63	Vehicle position unchanged; continue 2nd APXS analysis of Half Dome (A-19)
64	SVP X=-4.896, Y=-3.833, H=87.49; complete 2nd APXS analysis of Half Dome (A-19); retract APXS; deploy APXS; RC mosaic of Moe; start APXS analysis of Moe (A-20) (X=-4.20, Y=-4.10, Z=-0.38)
65	Vehicle position unchanged; APXS analysis of Moe (A-20)
66	SVP X=-4.381, Y=-3.693, H=130.08; retract APXS; deploy APXS; RC mosaic of Moe; APXS measurement of atmosphere (A-21)
67	SVP X=-4.394, Y=-3.677, H=130.00; retract APXS; deploy APXS; RC mosaic of Stimpy; rover climbed Stimpy so that APXS sampled air (A-22)
68	SVP X=-3.838, Y=-3.663, H=140.33; retract APXS; RC mosaic image of APXS on Stimpy; deploy APXS; start APXS analysis of Stimpy (A-23) (X=-3.48, Y=-3.86, Z=-0.43)
69	Vehicle position unchanged; continue analysis of Stimpy
70	SVP X=-3.683, Y=-3.534, H=137.50; retract APXS (from A-23); soil mechanics experiment for tare (no load current) because rover climbed Stimpy and wheel appeared to be above surface; LR wheel 1.0 turns forward and then 1.0 turns backward (T-8); LF and RF camera mosaic images of Moe; LF and RF camera mosaic images of Stimpy
71	SVP X=-4.240, Y=-3.770, H=219.00; LF and RF camera images of Half Dome; LF and RF camera mosaic images of Shark
72	SVP X=-4.792, Y=-2.625, H=134.00; LF and RF images of surface; LF and RF camera mosaic images of Chimp
73	Vehicle position unchanged, no uplink or downlink
74	SVP X=-8.932, Y=-1.566, H=254.91; closeup imaging of Chimp; two RF images of Chimp; soil mechanics experiment; RR wheel 1.5 turns forward (S-14) (X=-11.50, Y=-3.01)
75	SVP X=-11.502, Y=-3.006, H=302.43; LF and RF camera images of swale area and North Peak; LF and RF camera images of west swale area
76	SVP X=-11.228, Y=-3.087, H=131.04; LF and RF camera images of west swale area; LF and RF camera images of Twin Peaks; deploy APXS; RC image of APXS in atmosphere; APXS of atmosphere (A-24)
77	SVP X=-9.557, Y=-1.543, H=15.00; APXS of atmosphere (A-24); deploy APXS; RC image of APXS site; APXS of atmosphere (A-25)
78	SVP X=-9.369, Y=-2.20, H=24.00; APXS of atmosphere (A-25); deploy APXS; RC image of APXS in air above Chimp; APXS of atmosphere (A-26)
79	SVP X=-8.865, Y=-2.108, H=65.10; APXS of atmosphere (A-26); position APXS; RC image of APXS on Chimp; APXS of Chimp (A-27) (X=-9.03, Y=-2.59, Z=-0.07)
80	Vehicle position unchanged; APXS of Chimp (A-27)
81	Vehicle position unchanged; APXS of Chimp (A-27); RC image of APXS on Chimp
82	APXS of Chimp (A-27)
83	Vehicle position unchanged, partial downlink

Standard soil mechanics experiments include three rear and three front camera images. RC, rear color; RF, right front; LF, left front; RR, right rear; LR, left rear; X, Y, and Z values give the center position of the rover or APXS target in meters, in the Mars Local Level coordinate frame. X is north, Y is east, and Z is down (also in meters), with origin in the center of the lander baseplate. H is the heading of the rover in degrees (0 is north, 90 is east). SVP, set vehicle position command uplinked to the rover (actual position at beginning of sol and end of previous operational sol, measured from IMP stereo pair images of the rover).

## 6.7. ASI/MET Operations and Data Sets

The ASI/MET experiment, which consisted of accelerometer and MET instruments, collected data throughout the entry, descent and landing, and landed phases of the Mars Pathfinder mission. During entry, descent, and landing, the primary goal of the accelerometer instrument was to measure deceleration during entry, before parachute release. Vertical profiles of atmospheric density, pressure, and temperature from 150 to 10 km were derived from these measurements. The primary goal of the MET instrument was to measure vertical profiles of atmos-

pheric pressure and temperature directly, after heat shield separation at about 7.5 km, as the lander descended by parachute [Seiff *et al.*, 1997].

Both the accelerometer and MET instruments were powered on 90 min before entry to allow them to stabilize and to acquire calibration data. At the beginning of the free-fall telemetry phase, 15 min before entry, science data collection began. The science accelerometer sampled acceleration in three orthogonal axes at a rate of 1 Hz during free-fall and 32 Hz during the entry, descent, terminal, and landing telemetry phases, ob-

**Table 7.** APXS Measurements

APXS Measure ment	Local True Solar Initial start	Local True Solar Final Stop	Integrated Measurement Time, hours	Spectra Accumulation Time, hours	Target	Comments
A-1	sol 1 0717	sol 2 0958	2.8	1.9	atmos.	Rover on lander, background calibration
A-2	sol 2 1453	sol 3 1000	19.6	15.9	soil	Near end of ramp. APXS deployment mechanism not quite touching the ground
A-3	sol 3 1500	sol 4 0701	16.5	13.6	rock	Barnacle Bill
A-4	sol 4 1659	sol 5 0132	8.8	8.1	soil	Soil 3 m from Yogi
A-5	sol 5 1601	sol 6 0655	15.3	9.2	soil	Soil 2 m from Yogi
A-6	sol 10 0901	sol 10 0940	0.7	0.1	atmos.	Electronics noise test, no other rover activities during APXS measurement
A-7	sol 10 1417	sol 11 0237	12.7	5.7	rock	Yogi
A-8	sol 14 1403	sol 15 0255	13.2	5.7	soil	Scooby Doo
A-9	sol 15 1404	sol 16 0315	8.6	7.7	soil	Disturbed soil next to Scooby Doo. APXS deployment mechanism a few cm above the ground
A-10	sol 20 1403	sol 21 0259	8.3	7.0	soil	Dark soil next to Lamb
A-11	sol 22 1523	sol 23 0240	11.6	4.8	atmos.	APXS didn't land on rock, measured atmosphere above Souffle instead
A-12	sol 24 1707	sol 24 1717	0.2	0.1	atmos.	Electronics noise test while APXS is running on shared solar panel and battery power
A-13	sol 24 1801	sol 24 1812	0.2	0.1	atmos.	Electronics noise test while APXS is running on battery power
A-14	sol 25 0006	sol 25 0016	0.2	0.1	atmos.	Electronics noise test at night with the rover CPU turned on
A-15	sol 28 1405	sol 29 0244	8.0	5.3	soil	Mermaid dune
A-16	sol 37 1407	sol 38 0305	8.2	6.5	rock	Wedge
A-17	sol 52 1418	sol 53 0305	8.0	7.0	rock	Shark
A-18	sol 55 1406	sol 56 0005	7.2	5.9	rock	Half Dome
A-19	sol 58 1208	sol 64 1045	12.6	8.9	rock	Half Dome, another location. Rover battery died sol 56 and it took several days to recover
A-20	sol 64 1204	sol 66 1040	10.3	6.5	rock	Moe
A-21	sol 66 1204	sol 67 1032	5.2	3.0	atmos.	
A-22	sol 67 1204	sol 68 09:32	4.0	2.0	atmos.	
A-23	sol 68 12:05	sol 70 1047	9.5	4.9	rock	Stimpy
A-24	sol 76 12:09	sol 77 0906	2.7	0.5	atmos.	
A-25	sol 77 12:08	sol 78 0906	3.0	0.8	atmos.	
A-26	sol 78 12:03	sol 79 1017	4.6	2.6	atmos.	
A-27	sol 79 12:08	sol 82 0947	11.1	6.3	rock	Chimp

Integrated measurement time is usually less than the measurement final stop time minus the initial start time, because the integrated time does not include quiet periods when the APXS was powered off. The APXS spectra accumulation time is embedded in the APXS spectral data files, and is less than integrated time because it includes detector dead time and electronics readiness. Measurement targets were either rock, soil, or atmosphere (atmos).

taining a total of 13,340 samples. Automatic and programmed gain changing ensured that all the measurements were on scale in spite of measured accelerations that ranged over 7 orders of magnitude. The MET instrument sampled temperatures and pressures once every 8 s during free-fall and entry. This sampling rate increased to 2 Hz during the descent and terminal telemetry phases, before falling to 1 Hz during landing. A total of 430 MET samples of pressure and temperature were taken during entry, descent, and landing [Schofield *et al.*, 1997].

After landing, the entire ASI/MET scientific data set was collected by the MET instrument [Schofield *et al.*, 1997]. The accelerometer instrument was used infrequently to help establish the attitude of the spacecraft. MET surface measurements were driven by two scientific goals: (1) to obtain a surface meteorological record of pressure, temperature, and wind velocity; and (2) to make temperature and wind observations suited to surface boundary layer studies. The meteorological record required measurements at all timescales with a good coverage of local time, whereas the boundary layer measurements required periods of continuous rapid sampling. As data rate and power limitations prevented continuous rapid sampling for an

extended period, MET surface observation strategy was a compromise between these two requirements.

The MET surface observation unit was a measurement session, defined principally by its duration and the parameter sampling rate. For each of the first 30 sols, 51 three min sessions with 4 s sampling rates equally spaced over the Martian day, provided the meteorological data record [Schofield *et al.*, 1997]. Longer 15 min and 1 hour sessions with 1 s sampling rates were interspersed between these measurements to provide boundary layer data. After sol 30, measurements were no longer made regularly at night to conserve power, and toward the end of the mission, temporal coverage had shrunk to just the morning hours. However, data volumes were not impacted by power concerns, and it became possible to sample data almost continuously during the daylight hours at either 4, 2, or 1 s rates. Finally, continuous 24 hour sampling at 4 s intervals was begun on sols 25, 32, 38, 55, and 68 and completed. More than 650,000 samples of 12 pressure, temperature, and wind sensor measurements in 1392 sessions were obtained during the 83 sol landed mission.

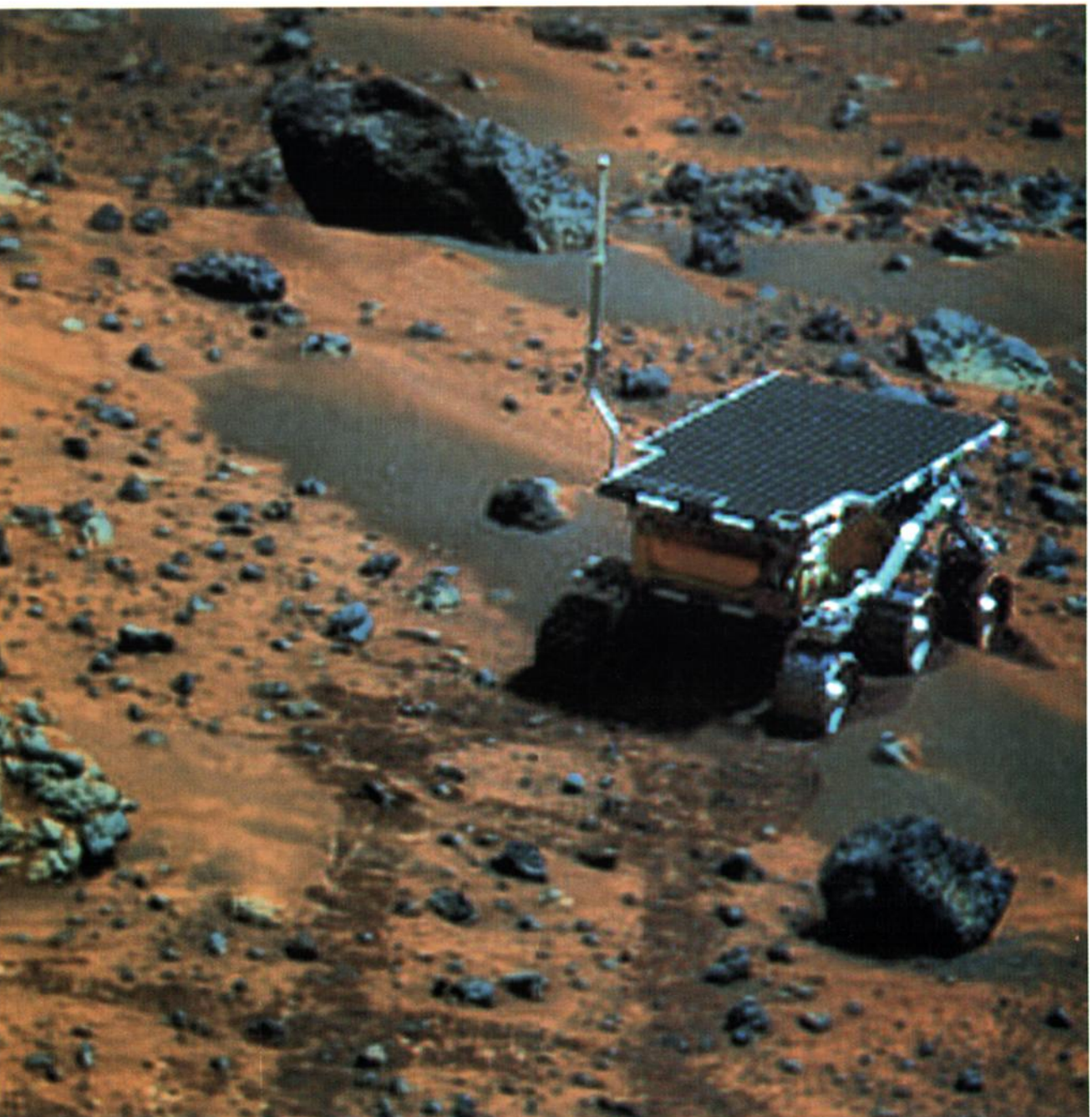


**Plate 7.** Color lander image of rover, facing the lander, on Mermaid Dune on sol 30. Mermaid Dune is covered by dark (gray) soil. Note the dark rocks, bright dust, disturbed soil exposed in rover tracks, as well as the dark soil. Note protruding lobes of the rock, Squash at the lower left of image, which resembles pillow basalts or autobreccias. Image compiled by co-adding two end-of-day rover IMP sequences to sharpen surface detail around the rover and reduce compression noise.

## 7. Overview of Science Results

### 7.1. Geology and Geomorphology

Many characteristics of the landing site are consistent with its being a plain composed of materials deposited by the Ares and Tiu catastrophic floods [Golombek et al., 1997b; Smith et al., 1997b], although alternative interpretations and combined processes involving floods, mass flows, and other processes have been suggested [Chapman and Kargel, this issue;

Tanaka, 1997, this issue]. The rocky surface (16% of the area is covered by rocks [Golombek et al., this issue]) is composed of subangular to subrounded pebbles, cobbles, and boulders that generally resemble depositional surfaces produced in terrestrial catastrophic floods, such as the Ephrata Fan in the Channeled Scabland of Washington State [Golombek et al., 1997a]. The Twin Peaks appear to be streamlined islands in lander images (Plate 3), consistent with interpretations of Viking Orbiter images of the region, which suggest the lander is

on the flank of a broad, gentle ridge trending northeast from Twin Peaks (Figure 4). This ridge is the rise to the north of the lander; it is aligned in the downstream direction from the Tiu Vallis floods, suggesting it is a debris tail deposited in the wake of Twin Peaks. Rocks in the Rock Garden (Shark, Half Dome, and Moe) may be imbricated or inclined blocks generally tilted in the direction of flow (Plates 3 and 5). Troughs visible throughout the scene may be primary features produced by the flood or they may result from the late-stage drainage of water after deposition, which preferentially carried away the fines, leaving a blocky armored surface behind (analogous to channels and surfaces present on the Ephrata Fan). Large rocks ( $>0.5$  m) appear tabular and surrounded and many are perched, consistent with deposition by a flood. They generally appear redder than smaller ( $<0.3$  m) more equant angular darker rocks and blocks that may be ejecta from Big Crater, about 2 km to the south. The difference in color may be due to the difference in time that the rocks have been on the surface collecting dust or undergoing surface weathering.

The general characteristics of the site are consistent with predictions that the site would be safe for landing and roving and less dusty than the Viking sites based on remote sensing data at scales of kilometers to tens of kilometers [Golombek et al., 1997a, b, this issue]. The prediction that the site would be a rocky plain, composed of materials deposited by a catastrophic flood, is consistent with that found at the surface and implies that some geologic processes observed in orbiter data can be used to infer surface characteristics where those processes dominate over other processes affecting the Martian surface. Lander and close-up rover images described later show a variety of rock morphologies, surface textures, and fabrics, suggesting that a variety of rock types are present (see later discussion), consistent with it being a "grab bag" of materials deposited by the flood.

There is abundant evidence for eolian activity at the site [Smith et al., 1997b; Greeley et al., this issue], although the overall effect on the surface seems to have been small, given that it still appears similar to when it formed in the Late Hesperian/Early Amazonian [Parker and Rice, 1997; Nelson and Greeley, this issue]. This argues that the erosional and/or depositional processes in the past 1.8–3.5 Gyr at the site have been minimal [Ward et al., this issue]. Wind tails, found behind some rocks (e.g., Barnacle Bill), cobbles and pebbles, and ripples and duneforms have all been imaged at the landing site. The material appears to be composed of very fine grained bright drift material [Rover Team, 1997a; Moore et al., this issue], similar in color (light yellowish brown [Maki et al., this issue]) to the dust in the atmosphere [Smith et al., 1997b; Thomas et al., this issue (a)]. Soil covering the lower 5–7 cm of several rocks such as Flat Top and Stimpy suggests that they have been exhumed [Smith et al., 1997b; Greeley et al., this issue]. This suggests that the landing area has been scoured by the winds and thus is a zone of net erosion and removal of surface fines. Some rocks appear similar to ventifacts on Earth, which are characteristically fluted and grooved by saltating sand-size particles in the wind [Bridges et al., this issue]. Although some possible ventifacts have been suggested at the Viking lander sites, they are not as well developed (or even as positively identified) or as pervasive as at the Pathfinder site [Bridges et al., this issue]. Ventifacts suggest abrasion by solid (crystalline) sand-size particles as opposed to poorly bound aggregates [Greeley et al., this issue]. Some duneforms in view of the lander and barchanoid dunes in the trough

behind the Rock Garden (imaged by the rover) are likely composed of sand or sand-size aggregates of fines that formed by saltation. The landing area has no obvious dunes visible in Viking orbiter images, so that their presence may suggest an abundance of sand-size particles on Mars, which appears consistent with recent Mars Orbiter Camera high-resolution images returned by Mars Global Surveyor [Malin et al., 1998]. Sand on Earth typically forms via fluvial processes that mechanically break down rocks into smaller fragments. In addition, their bright color in images suggests they might be composed of common light minerals such as quartz or feldspar, which may be another indicator of differentiated crustal materials on Mars (see later discussion). Alternatively, the dunes could be inactive and covered by a layer of bright dust or composed of sand-size clumps of clay-rich aggregates or other light-colored minerals. In general, wind directions from the orientations of wind tails and dunes on the surface agree with wind streaks in orbiter images and the orientation of the strongest winds (from the northeast) from global circulation models [Greeley et al., this issue], but not with the orientations of ventifacts [Bridges et al., this issue]. No changes at the site attributable to surface-atmosphere interactions were observed during the 83 sol life of the mission, suggesting that eolian activity occurs at other seasons when wind velocities are higher.

## 7.2. Mineralogy and Geochemistry

A variety of soil and dust deposits at the surface have been identified from spectral (0.4–1  $\mu\text{m}$  bands) mapping of the surface [Bell et al., 1998; Johnson et al., 1998]. The most abundant soil spectral units are (Plate 7) bright soil (very red, poorly crystalline eolian drift deposits), dark soil (grayer, perhaps coarser-grained deposits), and disturbed soil (darker deposits, uncovered by the action of rover wheels and air bag bounce/retraction). Rarer, localized soil spectral units include brown soil (a possibly more crystalline unit occurring primarily near the rock Lamb), pink soil (such as Scooby Doo and Bakers Bench, which was resistant to rover wheel scratching and may be an indurated soil or hardpan because its composition is similar to soils elsewhere at the site), and the magnetic dust that adhered to the magnetic properties experiment (described below). In general, the imaging results appear consistent with poorly crystalline or nanophase ferric-bearing materials, which is consistent with telescopic results. Elemental compositions of soil units measured by the APXS are generally similar to those measured at the Viking sites, with the possible exception of sulfur and titanium [Rieder et al., 1997b]. Because the Pathfinder and Viking landers are distributed around the planet, the similarities in soil compositions suggest that the compositions are influenced by globally distributed materials on Mars, such as the airborne dust. The similarity in compositions among the soils implies that the differences in color may be due to either slight differences in iron mineralogy or differences in particle size and shape and that the soils are likely complex mixtures of a variety of weathering products [Bell et al., 1998].

The magnetic properties experiment shows that airborne magnetic dust has been progressively deposited with time on most of the magnetic targets on the lander [Hviid et al., 1997; Madsen et al., this issue]. The dust is light yellowish brown [Maki et al., this issue] (the same color as the bright soil



**Figure 11.** Image of lander on Mars taken from rover left front camera on sol 33. The IMP (on the lattice mast) is looking at the rover. Air bags are prominent, and the meteorology mast is shown to the right. Lowermost rock is Ender, with Yogi on the other side of the lander. Notice the rough, nubby, or bumpy texture of Ender, which could be due to clasts within the rock or the result of chemical or eolian weathering of the rock. JPL logo is visible on the side of the electronics box, adjacent to the American flag.

[Smith *et al.*, 1997b; Johnson *et al.*, this issue] and that in the atmosphere [Thomas *et al.*, this issue (a)]) and has a magnetization and chemistry consistent with composite clay-sized silicate particles with a small amount (6% of the bulk, and roughly one third of the total iron oxide) of a very magnetic mineral, believed to be maghemite as stain or cement. The favored interpretation of these results is that iron was dissolved out of crustal materials in water, suggesting an active hydrologic cycle at some time on Mars, and that the maghemite is a freeze-dried precipitate [Hviid *et al.*, 1997; Madsen *et al.*, this issue].

In general, rocks are dark gray with discontinuous coatings of bright dust and/or weathered surfaces [Rieder *et al.*, 1997b; McSween *et al.*, this issue]. The rocks fall into four main spectral types: gray, red, pink and maroon. The first three form a spectral trend that includes the soil and dust deposits at the site. The maroon rocks occur as subrounded boulders in the far field, and appear coated with darker red or brown dust or soil, with which they form a second spectral trend [McSween *et al.*, this issue]. It is not known what type of rocks (igneous, sedimentary, or metamorphic) are present at the landing site, because close-up images of surface textures and fabrics, lander camera spectra, and rock chemistry have not allowed the unique identification of rock mineralogy or petrology. The

rock chemistry measured by the APXS is similar to basalts, basaltic andesites, and andesites on Earth. Generally, linear relationships between the red/blue ratio of the rocks, their silica or sulfur content, and the average soil composition suggest that dark high silica rocks are coated with sulfur-rich bright reddish dust. This relationship allows a dust- (and sulfur-) free rock composition to be calculated, which is andesitic in composition (similar to the dark rock Shark) and distinct from the mafic and relatively silica-poor Martian meteorites. The chemistry and normative mineralogy of the sulfur-free rock are similar to those of common terrestrial anorogenic andesites, such as icelandites, which formed by fractional crystallization of mantle derived parent materials [McSween *et al.*, this issue].

Rover close-up and lander super resolution images show rocks with a variety of morphologies, textures, and fabrics, such as pitted, smooth, bumpy, layered, and lineated [McSween *et al.*, this issue], suggestive of a variety of rock types. Many of the rocks are pitted (e.g., Flat Top, Barnacle Bill, Souffle, and the Dice) and resemble vesiculated volcanic rocks, which further argues for a volcanic origin, although alternative processes such as chemical etching and eolian abrasion could also be responsible. Other rocks appear to have subtle 3-5 mm thick light-dark layers (e.g., Chimp, Zebra, Ender, and Mini-Matterhorn) that could be sedimentary layers, volcanic flow

banding, or metamorphic foliation (Figure 11). Squash (Plate 7) shows large resistant protruding knobs or lobes separated by lighter color indented, possibly weathered zones reminiscent of pillow basalts on Earth, where magma freezes in water, although other origins such as an autobreccia or a sedimentary or volcanic rock or breccias with large clasts are also possible. Rocks with a bumpy texture (with bumps of a few millimeters across) are common (e.g., Shark). Prince Charming has been suggested to be a conglomerate composed of rounded pebbles with reflective hemispheric pockets or indentations where pebbles originally embedded in a finer matrix have fallen out [Rover Team, 1997a]. Rocks such as these could be the source of numerous loose rounded pebbles and cobbles on the surface. Alternative origins for these rocks and textures include volcanic agglomerates or breccias with wind-eroded pits. If the rocks are conglomerates, they require running water to smooth and round the pebbles and cobbles over long periods of time. The rounded materials would then be deposited into a finer grained (sand and clay) matrix and lithified before being carried to the site. They support a warmer and wetter past in which liquid water was stable and the atmosphere was likely thicker.

Geologic maps of the region as well as likely transport distances by the floods do not allow unambiguous interpretations of the mapped units from which the rocks at the site have been carried. Both ridged plains and ancient heavily cratered terrain are located at similar distances near the mouth of the channel [e.g., Rotto and Tanaka, 1995], and they may underlie and therefore have been locally eroded to form the channel in the area of the landing site. The simplest explanation is that the high silica rocks are volumetrically minor volcanic differentiates [McSween *et al.*, this issue] from the ridged plains, which have been interpreted to be basaltic. If these rocks are samples of the ancient heavily cratered terrain, they suggest widespread differentiated crust on Mars, similar to continental crust on Earth. If the putative conglomerates and/or other sedimentary rocks are from the ancient highlands, then they require an earlier more clement Mars, which is consistent with some interpretations of erosion of heavily cratered terrain in Viking images; if they are samples of younger Hesperian-aged terrain, then they may suggest a clement period relatively late in Martian history, which may be more difficult to explain.

### 7.3. Surface Material Properties

Observations of wheel tracks and soil mechanics experiments suggest that a variety of materials with different physical properties are present at the landing site [Rover Team, 1997a]. Rover tracks in bright drift material and others preserve individual cleat marks that are reflective, indicating that they are compressible deposits of very fine grained dust. This drift material forms the wind tails and other fine eolian features, suggesting it is the same fine dust that is suspended in the atmosphere. Cloddy deposits may be fluvial in origin or due to a combination of processes [Moore *et al.*, this issue]. After digging holes in these deposits, they appear to be composed of poorly sorted dust, sand-size particles, lumps of soil, and small rock granules and pebbles. These deposits have small cohesions and large angles of internal friction. Measurements of angles of repose and internal friction by the interaction of these materials with the rover wheels are like soils on Earth and imply bulk densities near  $1.5 \text{ g/cm}^3$ . Soil mechanics experiments and imaging of holes dug in Mermaid Dune (Plate 7)

suggest it may be a fluvial feature of poorly sorted materials with an eolian lag of dark gray sand and rock granules. Intermittent thick coatings of dust on the rover wheels suggest that the dust becomes electrostatically charged when compressed (Ferguson *et al.*, this issue).

### 7.4. Atmosphere Science

The ASI measured the density, pressure, and temperature during entry, descent, and landing at  $L_s 143^\circ$  in late northern summer. The upper atmosphere (above 60 km altitude) was on average 20 K colder than measured by Viking [Schofield *et al.*, 1997; Magalhães *et al.*, this issue]; this appears consistent with seasonal variations and entry at 0300 local solar time (compared with the warmer upper atmosphere measured by Viking at 1600 local solar time). Below 60 km, temperatures were a little higher than Viking above 35 km and fairly similar to those measured by Viking below. At 80 km above the surface, the temperature recorded is actually below the  $\text{CO}_2$  condensation temperature, which suggests nighttime carbon dioxide clouds are possible [Magalhães *et al.*, this issue]. The profile also shows evidence for wave structure, perhaps due to thermal tides that propagate up through the atmosphere [Magalhães *et al.*, this issue]. The lower atmospheric temperatures are consistent with a dusty lower atmosphere [Schofield *et al.*, 1997; Haberle *et al.*, this issue] and the measured total opacity of 0.5 from the surface by the IMP [Smith and Lemmon, this issue]. At 10 km altitude, a temperature minimum at the base of an elevated thermal inversion [Magalhães *et al.*, this issue; Haberle *et al.*, this issue] is colder than the condensation temperature for a 10 precipitable micron ( $\text{pr } \mu\text{m}$ ) column abundance of water vapor. This altitude is consistent with the estimated height of ubiquitous early morning white to blue water ice clouds that appear to sublime away later in the morning [Smith *et al.*, 1997b; Smith and Lemmon, this issue].

The meteorology measurements show repeatable diurnal and higher order pressure and temperature fluctuations [Schofield *et al.*, 1997]. Daily pressure fluctuations show strong semidiurnal oscillations that are also indicative of a dusty lower atmosphere. The barometric minimum was reached at the site near sol 20, indicating the maximum extent of the winter south polar cap, which is composed of frozen carbon dioxide. Weather systems moved across the lander late in the mission and are likely eastward traveling baroclinic waves. Daily temperature measurements showed a predominantly diurnal cycle (with a 263 K maximum at 1400 local time and a 197 K minimum just before sunrise at 1 m altitude). In the morning, however, temperatures fluctuated abruptly up to 20 K with time and up to 10 K between 0.25 and 1 m height. These measurements suggest that cold morning air was being warmed by the surface and was convecting upward in small eddies. Afternoon temperatures, after the atmosphere has been warmed, do not show these variations. Wind speeds were low (<10 m/s) and variable; wind direction was from the south for most of the night and then rotated clockwise completely around (through west, north, and east) returning to south at night due to tidal and upslope and downslope effects. Small-scale vortices were detected repeatedly from midmorning to midafternoon from a pronounced short pressure drop, with opposite relatively high winds before and after [Schofield *et al.*, 1997]. Pathfinder may have imaged them as dusty V-shaped to conical features (dust devils) tens of meters wide and hundreds of meters high [Metzger *et al.*, 1998], and the solar power dropped during the passage of one,

further indicating that they entrain dust and thus may be a means of lifting dust into the atmosphere.

The sky has been a light yellowish brown color due to dust particles in the atmosphere (Plate 3), similar to what was seen by the Viking landers [Maki *et al.*, this issue]. The total optical depth, which was measured by direct observations of the Sun during the day (at wavelengths of 450, 670, 883, and 989 nm) and stars at night, was found to be about 0.5 at the time of landing and increased slowly during the mission [Smith and Lemmon, this issue]. It was highest in the early morning, particularly in the blue, and decreased during the day (by up to 0.1), consistent with white to blue colored water ice clouds, observed before daybreak, but not later in the day [Smith *et al.*, 1997b]. Measurements of dust accumulation on a specially designed rover sensor and a general decrease in solar power on the solar cells are consistent with a 0.2% per day obscuration due to fallout of dust from the atmosphere [Rover Team, 1997a]. Filters in the IMP were used to investigate the 935 nm absorption of water vapor in the atmosphere. Values of  $6 \pm 4 \text{ pr } \mu\text{m}$  were found, with some indications that the water vapor was more concentrated at lower altitudes in the atmosphere [Titov *et al.*, this issue]. The sky brightness exhibited strong forward scattering and a relatively less red aureole about the Sun. Modeling of the distribution gives a mean cross-section weighted particle radius of around 1.5  $\mu\text{m}$  [Tomasko *et al.*, this issue; Markiewicz *et al.*, this issue]. The diffuse flux from the sky was strong (up to 50% of the direct flux at solar elevation angles of around 45°) and reddens the illumination of the surface significantly [Thomas *et al.*, this issue (a)], making the determination of the exact photometric behavior of rocks particularly complicated [Johnson *et al.*, this issue]. Spectra of Phobos and Deimos were obtained, showing these bodies to be similar to red C-type and D-type asteroids [Thomas *et al.*, this issue (b); Murchie *et al.*, this issue]. Geometric albedos of 0.065 and 0.068 were found, respectively, consistent with previous Viking orbiter observations.

### 7.5. Rotational and Orbital Dynamics

Daily Doppler tracking and less frequent two-way ranging during communication sessions between the spacecraft and Deep Space Network antennas have resulted in a solution for the location of the lander in inertial space and the direction and orientation of the Mars rotation axis [Folkner *et al.*, 1997b]. Combining this with earlier results from the Viking landers on the orientation of the pole of rotation and its change over the past 20 years allows the determination of the Mars precession rate ( $-7576 \pm 35$  milliarc seconds of angle per year). The precession rate allows calculation of the polar moment of inertia ( $0.3662 \pm 0.0017$ ), which is consistent with the hypothesis that the nonhydrostatic component is due to the Tharsis bulge. The estimated precession rate and moment of inertia (previously uncertain enough to not yield geophysically useful constraints [Bills and James, this issue]) constrain the radius of the central metallic core to be greater  $\sim 1300$  km but no larger than about 2000 km [Folkner *et al.*, 1997b]. It also rules out warm interior models with mantle compositions similar to Earth and cold, highly iron enriched mantle models. If the (iron-enriched) Shergottite meteorites are typical of the composition of the Martian mantle, then it must be warmer than Earth's (for the same pressure level) and the core radius must be larger than for other mantle compositions [Folkner *et al.*, 1997b]. The estimated annual variation in rotation agrees

with the expected seasonal mass exchange of carbon dioxide between the atmosphere and ice caps.

## 8. Summary

1. Pathfinder landed safely by bouncing over 15 times on one of the rockiest locations of Mars without suffering any air bag tears or ruptures, thereby successfully demonstrating an extremely robust and inexpensive landing system that was developed and built in a relatively short period of time.

2. The lander, rover, and instruments operated for about 3 months and returned 2.3 Gbits of new information, which allowed addressing seven broad science investigations: geology and geomorphology of the surface, mineralogy and geochemistry of rocks and soils, physical properties of surface materials, magnetic properties of airborne dust, atmospheric science and aerosols, and rotational and orbital dynamics of Mars.

3. Pathfinder is the best known location on Mars (located at  $19.13^\circ\text{N}$ ,  $33.22^\circ\text{W}$  in the USGS reference frame), having been clearly identified with respect to other features on the surface by correlating five prominent horizon features and two small craters in lander images with those in high-resolution orbiter images and in inertial space from two-way ranging and Doppler tracking. Comparing the two locations indicates that the USGS cartographic reference frame is displaced 18.15 km to the west and 8.78 km to the north from its inertial location ( $19.28^\circ\text{N}$ ,  $33.52^\circ\text{W}$ ).

4. Reconstruction of the final landing sequence indicates that the parachute/backshell/lander was tilted due to a northwest directed wind and wind shear, which resulted in the lander bouncing about 1 km to the northwest and initially downhill about 20 m from where the solid rockets fired. Two anomalously bright spots located in the lander scene are likely the heat shield, which continued in a ballistic trajectory about 2 km downrange (west southwest), and the backshell/parachute, which stayed nearer to where the rockets fired. Unconnected disturbed soil patches in the scene indicate that the final few bounces of the lander were from the east-southeast and were followed by a gentle roll to the west before coming to rest on the base petal. The location of the lander away from where the solid rockets fired and considerations of the exhaust products used to inflate the air bags and their fate indicate that the Pathfinder landing system is one of the cleanest designed, leaving the local area essentially contaminant free.

5. Because the lander and rover were solar powered, most real-time operations occurred during the Martian day, which shifted 37 min a day relative to time on Earth and involved 24 hour staffing during the nominal mission. Scientists and engineers had 3 hours from the end of the last downlink of a sol to analyze the data that had been returned, assess what had been learned, determine the actual location of the rover, and revise plans for the subsequent sol. The next 12 hours involved creating the specific lander, rover, and instrument sequences, fitting them in a workable timeline, testing and validating them on a test bed, and uplinking them to the spacecraft at the start of the next sol.

6. The rover explored about  $200 \text{ m}^2$  of the Martian surface in a 104 m traverse that circumnavigated the lander out to a distance of 12 m. It returned 564 images from the forward black and white stereo and rear color cameras and 16 chemical analyses of rocks and soils. It also performed 29 soil mechanics experiments and completed about 10 technology experiments.

7. The lander imager returned 16,635 images from the surface of Mars. Six major panoramas were obtained at various times and image compressions, including nearly lossless multicolor data from both the predeployed and postdeployed configuration. It also imaged various other objects including the wind socks, rover, magnetic, calibration, color, astronomical, and miscellaneous targets.

8. The vertical structure of the atmosphere from 150 km altitude to the surface was determined during entry and descent by accelerometer (13,340 samples) and pressure and temperature measurements (430 samples each). Surface meteorology measurements (pressure, temperature at three heights, and wind) were collected during the surface portion of the mission. During the nominal mission (first 30 sols), meteorology measurements were collected for 3 min at half hour intervals to characterize daily variations. Fifteen minute and 1 hour high-frequency (1, 0.5, and 0.25 Hz) sampling sessions were interspersed to characterize boundary layer and small-scale fluctuations. During 5 sols, data were collected continuously every 4 s for a complete Martian day.

9. The rocky surface observed by Pathfinder, the troughs, streamlined hills, and perched and imbricated rocks are all consistent with its being altered little since formation by catastrophic floods up to a few billion years ago. Eolian activity may have deflated the surface by ~3-7 cm and sculpted wind tails behind rocks, collected sand into dunes, and grooved and fluted rocks. Remote sensing data at a scale of generally greater than ~1 km and an Earth analog correctly predicted a rocky plain safe for landing and roving with a variety of rocks deposited by catastrophic floods that are relatively dust free.

10. Some rock chemistries have high silica contents similar to anorogenic andesites (or icelandites) that formed by differentiation of mantle derived melts by fractional crystallization. Rocks with higher red/blue ratios and lower silica appear coated by varying amounts of bright dust, which is richer in sulfur and lower in silica. Rover close-up and lander super resolution images show rocks with a variety of morphologies, textures, and fabrics, such as pitted, smooth, bumpy, layered, and lineated, suggesting that a variety of rock types are present at the site. Rounded pebbles and cobbles on the surface and in some rocks that also have pockets where pebbles may have been suggest these rocks may be conglomerates (although other interpretations such as volcanic agglomerates or breccias are also possible), which formed in fluvial environments in which liquid water rounded the clasts and deposited them in a finer sand and clay matrix. If these rocks are conglomerates, they support a warmer and wetter past, where liquid water was in equilibrium with the environment.

11. A variety of soil-like deposits are found at the site with different colors and textures. Their compositions are somewhat similar to soil at the Viking sites, suggesting they are complex mixtures of weathering products influenced by globally distributed materials, such as the airborne Martian dust. Bright dust appears to be deposited from the atmosphere; it is very fine grained and highly compressible. Other materials at the landing site are poorly sorted, are composed of dust-through pebble-sized grains, and may be fluvial in origin or due to a combination of processes. Airborne dust particles are composite silicates magnetized by a highly magnetic mineral interpreted to be maghemite; it may have been freeze dried as a stain or cement from liquid water that leached iron from crustal materials in an active hydrologic cycle.

12. In general, the atmosphere of Mars was similar to that experienced by Viking. The lower 60 km appears warm and dust rich (total opacity 0.5) with strong semidiurnal pressure oscillations. The atmosphere above is colder, likely due to the 0300 local time of entry. Dust particles are about 1.5  $\mu\text{m}$  in radius and 6±4 pr  $\mu\text{m}$  of water vapor was measured in the atmosphere. Water ice clouds appear early in the morning and sublimate away by midmorning, and surface temperatures in the morning showed large variations with time and height. Dust devils (small-scale vortices that appear to entrain dust) were detected repeatedly in the early afternoon when ambient winds were low and appear to have been imaged.

13. Regular two-way ranging and Doppler tracking during communication sessions between the spacecraft and Deep Space Network antennas have resulted in a solution for the location of the lander in inertial space and the direction and orientation of the Mars rotation axis. When combined with Viking results 20 years earlier, Pathfinder data allow the determination of the Mars precession rate and the moment of inertia, which constrains the central metallic core to be between ~1300 km and 2000 km in radius. The annual variation in rotation agrees with the expected seasonal mass exchange of carbon dioxide between the ice caps and atmosphere.

14. Taking all the results together supports an early Mars that may be Earth-like. Some crustal materials on Mars may be similar in silica content to continental crust on Earth. The rounded pebbles, cobbles, and the possible conglomerate and the abundant sand- and dust-size particles and models for their origin support a water-rich planet in which the early environment was warmer and wetter and liquid water was in equilibrium, perhaps similar to the early Earth. In contrast, Mars, since the Hesperian (1.8-3.5 Ga), appears to be a very un-Earth-like place, with very low erosion rates producing minor changes to the surface at the Pathfinder landing site.

**Acknowledgments.** This acknowledges the extraordinary effort put forward by the Mars Pathfinder team. Their dedication and work enabled this mission to obtain and return the data described herein and improve our knowledge of the Red Planet. Work described in this paper was carried out as part of the Mars Pathfinder Project at the Jet Propulsion Laboratory, California Institute of Technology, under contract with the National Aeronautics and Space Administration. We thank M Mellon and A Albee for comments on the manuscript.

## References

- Bell, J., et al., Mineralogy, composition, and origin of soil and dust at the Mars Pathfinder landing site, *Lunar Planet Sci.*, XXIX, Abstract #1723, 1998.
- Bills, B G, and T. S. James, Moments of inertia and rotational stability of Mars: Lithospheric support of subhydrostatic rotational flattening, *J. Geophys Res.*, this issue
- Bridges, N. T., R Greeley, A. F. C. Haldemann, K. E. Herkenhoff, M. Kraft, T. J. Parker, and A. W Ward, Ventifacts at the Pathfinder landing site, *J Geophys. Res.*, this issue.
- Chapman, M. G., and J. S. Kargel, Observations at the Mars Pathfinder Site: Do they provide "unequivocal" evidence of catastrophic flooding?, *J. Geophys. Res.*, this issue.
- Duxbury, T. C., Preliminary cartographic analysis of the Pathfinder landing site using Viking Orbiter images, in *Mars Pathfinder Landing Site Workshop II: Characteristics of the Ares Vallis Region and Field Trips in the Channeled Scabland, Washington*, edited by M. P Golombek, , K. S. Edgett, and J. W. Rice Jr pp. 35-36, LPI Tech. Rep., 95-01, Part 2, 47 pp., 1995.
- Folkner, W. M., R. D. Kahn, R. A. Preston, C. F. Yoder, E. M. Standish, J.G. Williams, C. D. Edwards, and R. W. Hellings, Mars dynamics from Earth-based tracking of the Mars Pathfinder lander, *J. Geophys. Res.*, 102, 4057-4064, 1997a

- Folkner, W. M., C. F. Yoder, D. N. Yuan, E. M. Standish, and R. A. Preston, Interior structure and seasonal mass redistribution of Mars from radio tracking of Mars Pathfinder, *Science*, 278, 1749-1752, 1997b.
- Ferguson, D. C., J. C. Kolecki, M. W. Siebert, and D. M. Wilt, Evidence for Martian electrostatic charging and abrasive wheel wear from the wheel abrasion experiment on the Pathfinder Sojourner rover, *J. Geophys. Res.*, this issue.
- Gaddis, L. R., et al., Digital mapping of the Mars Pathfinder landing site. Design, acquisition, and derivation of cartographic products for science applications, *J. Geophys. Res.*, this issue.
- Golombek, M. P., The Mars Pathfinder Mission, *J. Geophys. Res.*, 102, 3953-3965, 1997.
- Golombek, M. P., R. A. Cook, H. J. Moore, and T. J. Parker, Selection of the Mars Pathfinder landing site, *J. Geophys. Res.*, 102, 3967-3988, 1997a.
- Golombek, M. P., et al., Overview of the Mars Pathfinder Mission and assessment of landing site predictions, *Science*, 278, 1743-1748, 1997b.
- Golombek, M. P., H. J. Moore, A. F. C. Haldemann, T. J. Parker, and J. T. Schofield, Assessment of Mars Pathfinder landing site predictions, *J. Geophys. Res.*, this issue.
- Greeley, R., M. Kraft, R. Sullivan, G. Wilson, N. Bridges, K. Herkenhoff, R. O. Kuzmin, and M. Malin, Aeolian features and processes at the Mars Pathfinder landing site, *J. Geophys. Res.*, this issue.
- Haberle, R. M., M. M. Joshi, J. R. Murphy, J. R. Barnes, J. T. Schofield, G. Wilson, M. Lopez-Valverde, J. L. Hollingsworth, A. F. C. Bridger, and J. Schaffer, General circulation model simulations of the Mars Pathfinder atmospheric structure investigation/meteorology data, *J. Geophys. Res.*, this issue.
- Howington-Kraus, E., R. L. Kirk, B. Redding, and L. A. Soderblom, High-resolution topographic map of the Ares Tiu landing site from Viking Orbiter data, in *Mars Pathfinder Landing Site Workshop II: Characteristics of the Ares Vallis Region and Field Trips in the Channeled Scabland, Washington*, edited by M. P. Golombek, K. S. Edgett, and J. W. Rice Jr., p. 38, LPI Tech. Rep. 95-01, Part 2, 47 pp., 1995.
- Hviid, S. F., et al., Magnetic properties experiments on the Mars Pathfinder lander: Preliminary results, *Science*, 278, 1768-1770, 1997.
- Johnson, J. R., et al., Preliminary results on photometric properties of materials at the Sagan Memorial Station, Mars, *J. Geophys. Res.*, this issue.
- Kirk, R. L., et al., Digital photogrammetric analysis of the IMP camera images: Mapping the Mars Pathfinder landing site in three dimensions, *J. Geophys. Res.*, this issue.
- La Voie, S. K., et al., Processing and analysis of Mars Pathfinder science data at JPL's Science Data Processing Systems Section, *J. Geophys. Res.*, this issue.
- Madsen, M. B., et al., The magnetic properties experiments on Mars Pathfinder, *J. Geophys. Res.*, this issue.
- Magalhães, J. A., J. T. Schofield, and A. Seiff, Results of the Mars Pathfinder atmospheric structure investigation, *J. Geophys. Res.*, this issue.
- Maki, J. N., J. J. Lorre, P. H. Smith, R. D. Brandt, and D. J. Steinwand, The color of Mars: Spectrophotometric measurements at the Pathfinder landing site, *J. Geophys. Res.*, this issue.
- Malin, M. C., et al., Early views of the Martian surface from Mars Orbiter Camera of Mars Global Surveyor, *Science*, 279, 1681-1685, 1998.
- Markiewicz, W. J., R. M. Sablotny, H. U. Keller, N. Thomas, D. Titov, and P. H. Smith, Optical properties of the Martian aerosols as derived from Imager for Mars Pathfinder midday sky brightness data, *J. Geophys. Res.*, this issue.
- McSween, H. Y., et al., Chemical, multispectral, and textural constraints on the composition and origin of rocks at the Mars Pathfinder landing site, *J. Geophys. Res.*, this issue.
- Metzger, S. M., J. R. Carr, J. R. Johnson, M. Lemmon, and T. J. Parker, Dust devil vortices detected in Mars Pathfinder images - exploring the surface-atmosphere link (abstract), EOS Trans. AGU, 79, F537, 1998.
- Moore, H., D. Bickler, J. Crisp, H. Eisen, J. Gensler, A. Haldemann, J. R. Matijevic, F. Pavlics, and L. Reid, Soil-like deposits observed by Sojourner, the Pathfinder rover, *J. Geophys. Res.*, this issue.
- Murchie, S., N. Thomas, D. Britt, K. Herkenhoff, and J. F. Bell III, Mars Pathfinder spectral measurements of Phobos and Deimos: Comparison with previous data, *J. Geophys. Res.*, this issue.
- Nelson, D. M., and R. Greeley, Geology of Xanthe Terra outflow channels and the Mars Pathfinder landing site, *J. Geophys. Res.*, this issue.
- Oberst, J., R. Jaumann, W. Zeitler, E. Hauber, M. Kuschel, T. Parker, M. Golombek, M. Malin, and L. Soderblom, Photogrammetric analysis of horizon panoramas: The Pathfinder landing site in Viking orbiter images, *J. Geophys. Res.*, this issue.
- Parker, T. J., and J. W. Rice, Sedimentary geomorphology of the Mars Pathfinder landing site, *J. Geophys. Res.*, 102, 25,641-25,656, 1997.
- Reid, R. J., et al., IMP image calibration, *J. Geophys. Res.*, this issue.
- Rieder, R., H. Wänke, T. Economou, and A. Turkevich, Determination of the chemical composition of Martian soil and rocks: The alpha proton X-ray spectrometer, *J. Geophys. Res.*, 102, 4027-4044, 1997a.
- Rieder, R., T. Economou, H. Wänke, A. Turkevich, J. Crisp, J. Bruckner, G. Dreibus, and H. Y. McSween, The chemical composition of Martian soil and rocks returned by the mobile alpha proton X-ray spectrometer: Preliminary results from the X-ray mode, *Science*, 278, 1771-1774, 1997b.
- Rotto, S., and K. L. Tanaka, Geologic/geomorphic map of the Chryse Planitia region of Mars, U. S. Geol. Surv. Misc. Invest. Map, I-2241, 1:5M scale, 1995.
- Rover Team, Characterization of the Martian surface deposits by the Mars Pathfinder rover, Sojourner, *Science*, 278, 1765-1768, 1997a.
- Rover Team, The Pathfinder microrover, *J. Geophys. Res.*, 102, 3989-4001, 1997b.
- Schofield, J. T., J. R. Barnes, D. Crisp, R. M. Haberle, S. Larsen, J. A. Magalhães, J. R. Murphy, A. Seiff, and G. Wilson, The Mars Pathfinder atmospheric structure investigation/meteorology (ASI/MET) experiment, *Science*, 278, 1752-1758, 1997.
- Seiff, A., et al., The atmosphere structure and meteorology instrument on the Mars Pathfinder lander, *J. Geophys. Res.*, 102, 4045-4056, 1997.
- Smith, P. H., and M. T. Lemmon, Opacity of the Martian atmosphere measured by the Imager for Mars Pathfinder, *J. Geophys. Res.*, this issue.
- Smith, P. H., et al., The Imager for Mars Pathfinder experiment, *J. Geophys. Res.*, 102, 4003-4025, 1997a.
- Smith, P. H., et al., Results from the Mars Pathfinder camera, *Science*, 278, 1758-1765, 1997b.
- Stoker, C. R., E. Zbinden, T. T. Blackmon, B. Kanefsky, J. Hagen, P. Henning, C. Neveu, D. Rasmussen, K. Schwehr, and M. Sims, Analyzing Pathfinder data using virtual reality and superresolved imaging, *J. Geophys. Res.*, this issue.
- Tanaka, K. L., Sedimentary history and mass flow structures of Chryse and Acidalia Planitia, Mars, *J. Geophys. Res.*, 102, 4131-4149, 1997.
- Tanaka, K. L., Debris-flow origin for the Simud/Tiu deposit on Mars, *J. Geophys. Res.*, this issue.
- Thomas, N., W. J. Markiewicz, R. M. Sablotny, M. W. Wuttke, H. U. Keller, J. R. Johnson, R. J. Reid, and P. H. Smith, The color of the Martian sky and its influence on the illumination of the Martian surface, *J. Geophys. Res.*, this issue (a).
- Thomas, N., D. T. Britt, K. E. Herkenhoff, S. L. Murchie, B. Semenov, H. U. Keller, and P. H. Smith, Observations of Phobos, Deimos, and bright stars with the Imager for Mars Pathfinder, *J. Geophys. Res.*, this issue (b).
- Titov, D. V., W. J. Markiewicz, N. Thomas, H. U. Keller, R. M. Sablotny, T. G. Tomasko, M. T. Lemmon, and P. H. Smith, Measurements of the atmospheric water vapor on Mars by the Imager for Mars Pathfinder, *J. Geophys. Res.*, this issue.
- Tomasko, L., R. Doose, M. Lemmon, P. H. Smith, and E. Wegryn, Properties of dust in the Martian atmosphere from the Imager for Mars Pathfinder, *J. Geophys. Res.*, this issue.
- Ward, A. W., L. R. Gaddis, R. L. Kirk, L. A. Soderblom, K. L. Tanaka, M. P. Golombek, T. J. Parker, R. Greeley, and R. O. Kuzmin, General geology and geomorphology of the Mars Pathfinder landing site, *J. Geophys. Res.*, this issue.
- Zeitler, W., and J. Oberst, The Mars Pathfinder landing site and the Viking control point network, *J. Geophys. Res.*, this issue.

R. C. Anderson, N. T. Bridges, R. A. Cook, D. Crisp, J. Crisp, W. M. Folkner, M. P. Golombek, J. A. Harris, A. F. C. Haldemann, K. E. Herkenhoff, P. H. Kallemeijer, J. N. Maki, R. M. Manning, J. Matijevic, T. J. Parker, T. P. Rivellini, J. T. Schofield, D. A. Spencer, S. W. Thurman, and R. M. Vaughan, Jet Propulsion Laboratory, 4800 Oak Grove Drive, California Institute of Technology, Pasadena, CA 91109-8099. (mgolombek@jpl.nasa.gov)

J. R. Barnes, College of Oceanic and Atmospheric Sciences, Oregon State University, Corvallis, OR 97331

J. F. Bell III and R. Sullivan, Center for Radiophysics and Space Research, 424 Space Sciences Building, Cornell University, Ithaca, NY 14853-6801. (jimbo@marswatch.tn.cornell.edu)

D T. Britt, M. Lemmon, R. Singer, P. H. Smith, and M.G. Tomasko, Lunar and Planetary Laboratory, University of Arizona, Tucson, AZ 85721. (britt@hindmost.lpl.arizona.edu)

J Brückner, R. Rieder, and H. Wänke, Max-Planck-Institut für Chemie, Saarstrasse, 23, Mainz 55122, Germany.

T Economou, Enrico Fermi Institute, University of Chicago, 933 East 56th, Chicago, IL 60637 (tecon@uchicago.edu)

R Greeley and G. Wilson, Department of Geology, Arizona State University, Tempe AZ 85287.

R. M. Haberle, A. Magalhães, J. R. Murphy, A Seiff, and C. Stoker, Ames Research Center, Moffett Field, Ca 94035

R B. Hargraves, Department of Geosciences, Princeton University, Princeton, NJ 08544

S F. Hviid, J. M. Knudsen, and M. B. Madsen, Niels Bohr Institute, Orsted Laboratory, Universitetsparken 5, DK-2100, Copenhagen O Denmark.

R. Jaumann, DLR, Institute of Planetary Exploration, Rudower Chaussee 5, 12489 Berlin Germany.

J. R. Johnson, R L. Kirk, L. A. Soderblom, and W. Ward, U.S. Geological Survey, 2255 North Gemini Drive, Flagstaff, AZ 86001. (johnson@flagmail.we.usgs.gov)

H. U. Keller, and N Thomas, Max-Planck-Institut für Aeronomie, Postfach 20, Katlenburg-Lindau, D-3411 Germany

S Larsen, Riso National Laboratory, AMY-125, P O. Box 49 Roskilde, Denmark DK-4000.

M. C Malin, Malin Space Science Systems, P.O. Box 910148, San Diego, CA 92191.

H Y McSween Jr , Department of Geological Sciences, University of Tennessee, 306 G&G Building, Knoxville, TN 37996-1410. (mcsween@utk.edu)

S. L Murchie, Applied Physics Laboratory, Johns Hopkins University, Laurel, MD 20723.

(Received March 9, 1998; revised June 29, 1998; accepted July 17, 1998.)